Review paper

Raman analysis of lipids in cells: Current applications and future prospects

Yixuan Zhou [a], Yuelin Xu [a], Xiaoli Hou [b, **], Daozong Xia [a, *]

[a] *School of Pharmaceutical Sciences, Zhejiang Chinese Medical University, Hangzhou, 310053, China*
[b] *Academy of Chinese Medical Science, Zhejiang Chinese Medical University, Hangzhou, 310053, China*

ABSTRACT

Lipids play an important role in the regulation of cell life processes. Although there are various lipid detection methods, Raman spectroscopy, a non-invasive technique, provides the detailed chemical composition of lipid profiles without a complex sample preparation procedure and possesses greater potential in basic biology, clinical diagnosis and disease therapy. In this review, we summarized the characteristics and advantages of Raman-based techniques and their primary contribution to illustrating cellular lipid metabolism.

1. Introduction

Lipids, as important biomolecular constituents, are involved in regulating cellular membrane structures, energy metabolism, cell signaling, and substance transportation [1]. Abnormal lipid metabolism is closely associated with the onset and progression of atherosclerosis, diabetes, obesity, Alzheimer's disease and cancer [2,3]. Conventional techniques for detecting cell lipids primarily include mass spectrometry (MS), fluorescence microscopy, and nuclear magnetic resonance (NMR) (Fig. 1). MS is widely used for identifying and quantifying cellular lipid composition. Coupled with liquid chromatography (LC) or gas chromatography (GC), MS can provide detailed information about lipid species, chain lengths and unsaturation levels [4]. However, MS requires typically complex procedures to obtain high-quality and high-concentration samples [5]. Fluorescence microscopy engages specific fluorescent dyes, such as Nile Red and BODIPY, to observe the distribution and dynamics of lipid droplets (LDs) [6], whereas detailed information about lipid species could not be provided. Additionally, fluorescent

signals might interfere with the normal function of lipids [7]. NMR offers a non-invasive method to study the chemical structure and dynamics of lipids [8], while the intrinsic limitations involve relatively low sensitivity as well as high requirements for sample preparation and experimental process.

In 1928, Indian physicist Chandrasekhara Venkata Raman discovered that approximately 1 in 10^7 scattered photons transfer a fraction of its energy to the material causing the scattering, a phenomenon known as Raman scattering (or inelastic scattering). When a photon scatters without a change in energy, it's termed Rayleigh scattering (or elastic scattering). The energy difference pre- and post-Raman scattering (ΔE) is known as the Raman shift. Stokes scattering occurs when the scattered light's frequency is lower than that of the incident light ($\Delta E < 0$), while anti-Stokes scattering happens when the scattered light's frequency is higher ($\Delta E > 0$). On the basis of the Raman scattering phenomenon, Raman spectroscopy quantifies the Raman shift (typically denoted in wavenumbers, cm^{-1}). Functioning as a chemical fingerprint, Raman spectroscopy provides information on the chemical structure, composition, quantity, crystal symmetry, and orientation of a sample [9] (Fig. 2). As a nondestructive and label-free vibrational spectroscopy technique, Raman facilitates the detection of intracellular lipids without sample damages and complex preparation [9]. This review elucidates the different Raman spectroscopy techniques commonly employed in biological
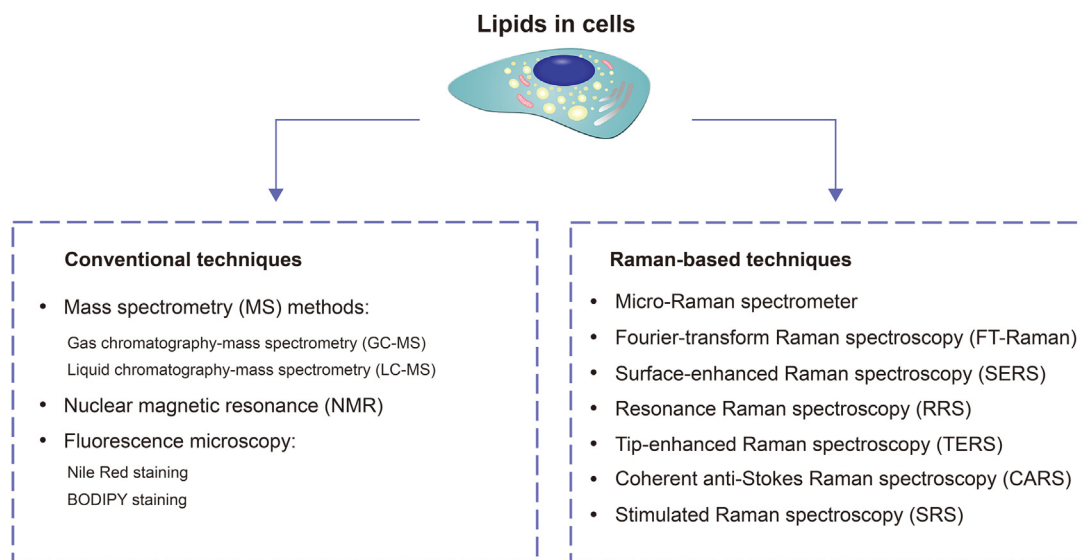

Fig. 1. Schematic representation of up-to-date techniques to identify cellular lipid profile.
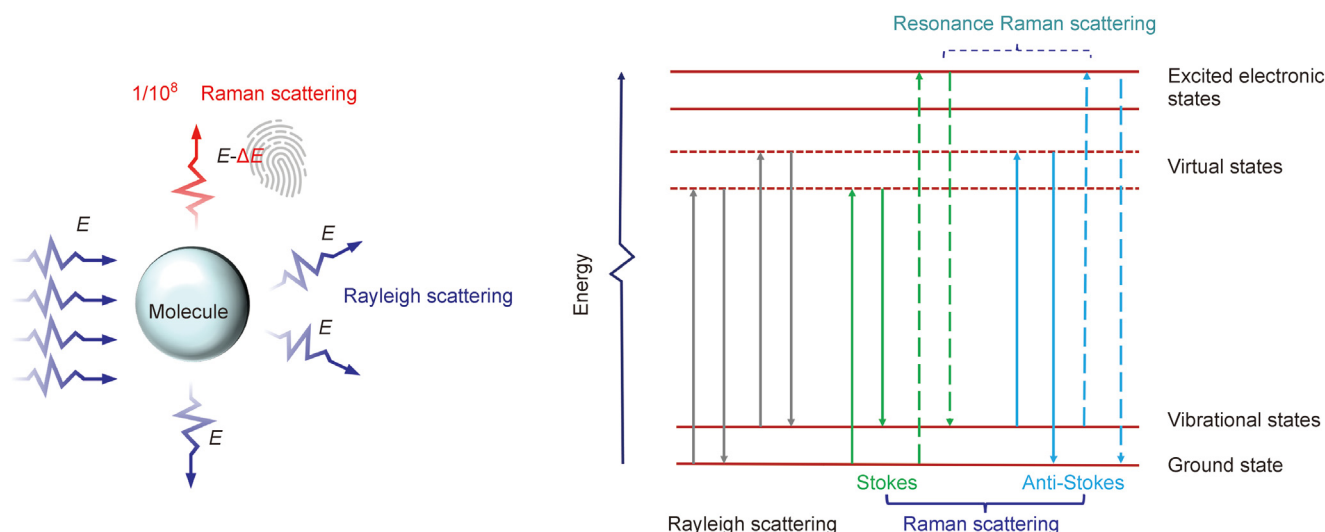

Fig. 2. Principles and energy-level diagrams of Rayleigh scattering and Raman scattering.

research and highlights their recent applications in cellular lipid metabolism.

2. Raman-based techniques as a tool for lipid analysis

The micro-Raman spectrometer, an integration of Raman spectroscopy and microscopy, facilitates high-resolution imaging and chemical analysis of samples. Fig. 3 shows the configuration of a typical laboratory micro-Raman spectrometer. Light from a laser passes through filters and coupling optics, reaches the objective lens, and is then focused onto the samples. Next, backscattered light from the samples is captured by the same objective lens and sent to the spectrometer, in which the light is dispersed into different wavelengths by a grating and detected by a charge-coupled device (CCD) camera. Raw data was converted into Raman spectra and Raman images using Raman spectrometer software.

Fourier-transform Raman spectroscopy (FT-Raman) integrates Fourier-transform techniques and Raman spectroscopy. Samples were excited by a near-infrared (NIR) laser (1,064 nm) in FT-Raman but not visible lights, leading to the reduction of the autofluorescence produced by excited lipids with visible lights [10]. It has been reported that FT-Raman data combined with chemometrics can effectively detect animal-originated feed samples and differentiate adulteration of diesel/biodiesel with vegetable oils [11,12]. The specific lipid peaks 2,875 and 2,836 cm^{-1} identified by FT-Raman corresponding to C−H symmetric stretching vibrations facilitate the discrimination of glioblastoma from meningiomas and other subtypes [13]. Similarly, in ovarian cancer, the lipid levels in platinum-resistant tissues are higher than those of sensitive controls, and peaks originating from lipid vibrations (2,817 and 1,714 cm^{-1}) could be used for distinguishing platinum-resistant and sensitive tissues [14]. The intensity of Raman scattering is proportional to the fourth power of the excitation light frequency (ν^4), and thereby scattering signals of FT-Raman spectroscopy are particularly weak due to the low frequencies of NIR lasers [15]. According to the approximate formula for spatial resolution: $d = 0.61\lambda/NA$ (d is the resolution limit, λ is laser wavelength, and NA is the numerical aperture of the
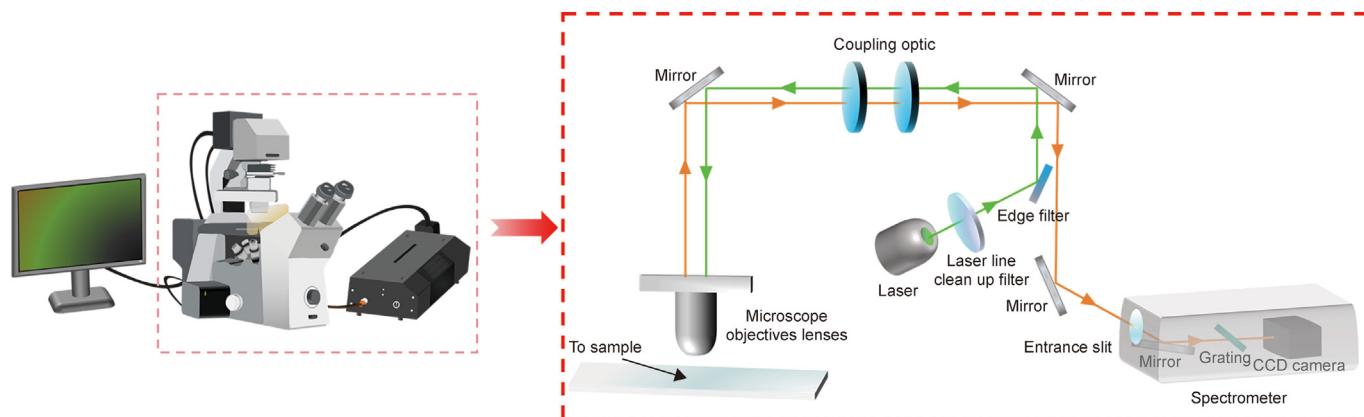
Fig. 3. Typical laboratory micro-Raman spectrometer. CCD: charge-coupled device.

objective lens), the spatial resolution of FT-Raman spectroscopy is relatively lower [16].

Surface-enhanced Raman spectroscopy (SERS) significantly enhances signals ranging from 10^5 to 10^{10}, through the excitation of localized surface plasmons induced by molecular adsorption on rough metal surfaces, colloids, or nanoparticles [17]. Thus, exceptional sensitivity and specificity were shown by SERS, particularly in the identification of lipid-based disease biomarkers and observation of drug delivery systems with low concentrations [18]. Using micron-nano composites as SERS substrates, Qi et al. [19] successfully monitored the externalization of phosphatidylserine (PS) on the cell membrane during the electrostimulation-induced apoptosis and revealed the dynamic difference in PS externalization between tumor and normal cells. Zhu et al. [20] explored the influence of metal nanoparticles on liposomal properties, including drug release and intracellular distribution. However, the poor reproducibility and stability of metal substrates increase the complexity of results interpretation [21].

When the frequency of the excitation laser coincides (or nearly coincides) with an electronic transition in the analyzed molecule, resonance Raman spectroscopy (RRS) is created and the signals are amplified accordingly (Fig. 1). This amplification makes the technique particularly suitable for detecting chlorophyll [22], carotenoids [22,23], and other colored lipid molecules [22]. The resonance Raman spectra of chlorophyll and carotenoids have been widely analyzed in the process of photosynthesis [22]. Based on the different Raman scattering efficiency of β-carotene and lycopene respectively at 488 and 514.5 nm excitation wavelength and the strong Raman peak corresponding to C=C vibration of the conjugate backbone of carotenoid molecules at 1,523 cm^{-1}, Blume-Peytavi et al. [24] found that oral supplementation with lycopene enhanced β-carotene and lycopene in human skin. The complex and expensive lasers matching electronic transitions of molecules are key points for RRS analysis, and consequently, limitations are manifested in the detection of molecules without distinct electronic transitions, especially in the analysis of complex clinical samples [25].

Tip-enhanced Raman spectroscopy (TERS), a sophisticated technique, combines scanning probe microscopy (like atomic force microscopy (AFM)) with Raman spectroscopy, which increases Raman signals around sharp metal tips composed of gold, silver, or copper. The greatest advantage of TERS lies in its ability to perform nanoscale imaging and spectroscopic analysis of lipids [26]. At the same time, the technique also remains challenging in capturing rapid dynamic alterations, such as lipid rearrangement or transport occurring on cellular membranes or subcellular structures, due to the relatively long scanning times required by scanning probe

microscopy [27]. The distance between the sample and probe as well as the probe shape also determines the intensities of TERS signals and affects the stability and reliability of this system. TERS is typically used in the analysis of the substructures extracted from cells or located just below the cellular membrane and cellular processes with slower dynamic changes [27], but not 3D reconstruction for the highly limited light field near the tip apex. For instance, TERS identified the cytochrome c protein structures in the mitochondria extracted from yeast cells, and typical phosphate residues of lipid molecules in the wavenumber ranges of 790–800 and 1,080 cm^{-1} were displayed [28]. TERS technology was used for imaging and chemical characterization of newly synthesized phospholipids within the smooth endoplasmic reticulum (ER) in pre-adipocyte cells due to the spatial resolution of less than 20 nm [29]. Additionally, the analysis of lipid membrane regions using TERS could determine extracellular vesicles (EVs) derived from red blood cells (RBCs) [30]. Pandey et al. [31] first utilized TERS to obtain label-free structural imaging of dipalmitoylphosphatidylcholine (DPPC) monolayers supported on Au metal tips.

Coherent nonlinear Raman imaging including coherent anti-Stokes Raman spectroscopy (CARS) and stimulated Raman spectroscopy (SRS), is established on the principal technique of two coherent excitation laser beams and nonlinear interactive method between two lasers and molecules [32]. Based on the very strong signal arising from CH_2 stretching vibration in lipid acyl chains, CARS and SRS are well suited to study lipid molecules directly *in vivo* [32]. CARS microscopy could image unstained lipids, especially concentrated vesicles like cytosolic lipid droplets (LDs) in which the high signal intensity potentiates dynamic observing [33]. Lipid structures in Caco-2 cells were imaged weekly using CARS microscopy at appropriate laser power settings (20–100 mW for the pump beam and 10–50 mW for the Stokes beam), and a significant increase in the quantity and size of LDs was observed over the 21-day cell culture period [34]. CARS signals display a non-resonant background at the anti-Stokes frequency which is independent of laser frequency tuning but related to the geometrical structure and local concentration of the object, and thereby image quality and detection sensitivity are inevitably compromised [32]. Moreover, CARS signals have a complex non-linear association with molecular concentration [32]. By contrast, SRS microscopy overcomes major hurdles of CARS. SRS signals are not only free from the non-resonant background but also linearly proportional to the analyte concentration, which is preferred for quantitative chemical analysis and high-precision imaging [35]. SRS microscopy showed that lipids were mainly stored in the intestine, hypodermis, oocytes and early-stage embryos of live *Caenorhabditis elegans*, and lipid

quantitative analysis was implemented [36]. Using SRS microscopy, the cellular distribution of CH_2 and CH_3 groups was captured at 2,950 and 2,850 cm^{-1}, respectively [37]. High-resolution 3D imaging was constructed by these specific peaks and automated image processing algorithms were used to quantify LD size, number, and spatial distribution within individual cells [37]. The study revealed that in non-adipocyte cells, such as HeLa cells, lipid accumulation primarily occurred through an increase of LD numbers but not size or lipid content following the addition of exogenous oleic acid [37]. Despite the advantages of SRS, SRS microscopy has detectability limitations for low-concentration analytes, primarily due to limited laser excitation power which cannot exceed the damage threshold, as well as the interference from non-Raman background which overwhelms the true SRS signals under low-concentration conditions [35]. Considering the advantages and disadvantages of CARS and SRS, researchers employed both techniques as complementary analyses. Borek-Dorosz et al. [38] employed CARS to investigate lipid distribution in endothelial cells according to the localization of lipid peaks at 2,850 cm^{-1}. Simultaneously, SRS imaging was used to obtain the subcellular localization of endogenous fatty acids (FAs) (at 2,930 and 2,850 cm^{-1}) and exogenous deuterated palmitic acid (D-PA) (at 2,110 cm^{-1}), and thereby the uptake of exogenous saturated FA was explored in inflamed endothelial cells [38].

3. Preparation of cell samples and optimization of data reproducibility in Raman spectroscopy

Raman microscopy is suitable for the detection of fixed cells. The common fixatives include alcohols and aldehydes, which correspondingly act by disrupting hydrophobic bonds in proteins or by inducing covalent bonds between proteins [39]. Typically, the cells were fixed for 4−15 min, and then washed with phosphate buffered saline (PBS) to remove any residual fixative for analysis. Thus, the different fixation procedures might influence cellular Raman spectral characteristics. Chan et al. [40] reported variations in band intensities related to DNA, RNA, proteins, and lipid vibrations among unfixed or fixed normal and leukemia cells. Specifically, only 60% of methanol-fixed cancer cells were accurately classified, while unfixed and formaldehyde-fixed cells achieved an accuracy of up to 99% [40]. Furthermore, 4% paraformaldehyde (PFA) fixation caused less alteration in CARS signal and protein/lipid content relative to ethanol fixation, and remained LD morphology and protein content comparable to that of living cells [41]. Therefore, 4% PFA effectively preserved cellular structure with minimal impact on lipids, suitable for cellular fixation in Raman analysis.

Raman microscopy also showed significant advantages in live cells. Due to the weak Raman intensity in a water medium, cells can be imaged in PBS or cell culture medium without fixation [39]. The 785 nm laser wavelength is usually employed in live cell studies, which minimizes sample degradation and photodamage even at higher powers and longer acquisition times. The unfixed adipocytes were imaged in PBS using CARS microscopy at a 785 nm laser, with incident laser powers of 62 mW (pump beam) and 6.5 mW (Stokes) [42]. During lipid imaging of MIAPaCa-2 cells by CARS microscopy, the Stokes beam and pump beam were respectively set as 1,040 and 800 nm corresponding to the Raman shift centered at 2,884 cm^{-1}, and water immersion objective lens (40 ×, NA = 0.8) was employed to enhance the focus of the laser beam [43]. Raman spectrometers coupled with a cell incubator were developed to support time-course observation of live cells [44].

The choice of Raman substrate significantly influences the quality and reliability of spectral data and plays a critical role in the measurement of cellular lipids. Currently, CaF_2 and BaF_2 are the most commonly used substrates in bio-spectroscopy due to their lack of characteristic Raman peaks in the cellular fingerprint spectral region (400−1,800 cm^{-1}) [45]. Despite the low background signal and high optical transmittance, the high cost of CaF_2 substantially hindered its application in the analysis of clinical samples. By contrast, glass and quartz substrates are more affordable, although cellular biological signals might be partially covered by the relatively high background signals. Suhito et al. [46] evaluated different substrates for Raman analysis, such as slide glass, silicate glass, and quartz. Slide glass exhibited peaks at 800 cm^{-1} which overlapped with certain cellular lipid peaks within the range of 900−1,200 cm^{-1}, while silicate glass showed strong fluorescent interference [46]. Quartz demonstrated weaker substrate peaks around 600 cm^{-1} and 750−850 cm^{-1}. Moreover, good biocompatibility between stem cells and quartz substrates was displayed and cellular proliferation was unaffected [46]. Quartz substrate was suitable for long-term monitoring of live cells using the Raman technique [46]. Metal substrates, such as gold and silver, are typically used to detect low-abundance lipids by SERS analysis. However, the release of metal ions might have a negative impact on cellular viability [18]. Gargotti et al. [47] analyzed HeLa cells and HaCaT cells cultured on three different substrates: conventional polystyrene cell culture dishes, CaF_2 slides, and glass slides coated with rat tail collagen to simulate the extra-cellular matrix (ECM) environment. Collagen is an ideal substrate for Raman spectral measurements for a prolonged cell by absorbing cell culture medium and minimal disruption of the cellular cycle compared with standard polystyrene dishes and CaF_2 substrate [47].

Valid data is crucial for the determination of cellular lipids using Raman spectroscopy. Control groups are firstly required to ensure the reproducibility of data, including the untreated group and positive standard group. These controls provided a negative or positive standard for subsequent data analysis to verify the accuracy of experimental results. Raman spectral characteristics of the untreated control group were compared with those from the specific treatment group (e.g., drugs, staining) to acquire significant alterations related to the stimulation, whereas results interpretation was validated by Raman spectra from the positive standard group to confirm the occurrence and relative concentration of specific lipids in the treatment group. Secondly, experimental conditions, such as cell source, cell density, treatment methods and observation time, should be consistent to minimize variability during sample preparation. Thirdly, calibration of the Raman spectrometer should be executed before each experiment by standard samples with known concentrations or commercially available Raman calibration materials, such as silicon wafers. Calibration with silicon wafers is crucial to ensure the instrument's sensitivity and accuracy, which produces a distinct sharp Raman peak at 521 cm^{-1} [48]. It is also recommended to keep a record of the instrument's status and environmental conditions during each experiment because temperature fluctuations may lead to shifts in Raman spectra by changing the position and intensity of peaks [49].

4. Major data analysis tools and methods for Raman spectroscopy

Rapidly processing spectra data and extracting relevant information with the assistance of computational algorithms promote the application of Raman spectroscopy in a wide range [50]. Commercial software, such as LabSpec, Renishaw WiRE, and Witec, are adopted by Horiba Jobin Yvon, Renishaw, and Witec company, separately [51−53]. Origin, a common graphing and data analysis software, also has a module for Raman analysis [54]. MATLAB [55] and LabVIEW [56] are specialized custom software applications.

The initial data preprocessing includes baseline correction, denoising, and normalization, which facilitate the increase of the

signal-to-noise ratio and comparability [53]. Baseline correction eliminates background signals using algorithms such as polynomial fitting and least squares [52]. Denoising employs methods like Gaussian filtering, mean filtering, and Savitzky-Golay filtering to smooth the data [51]. Normalization techniques, such as area and vector normalization, help standardize the spectral data [50]. Peak fitting completed via Gaussian-Lorentzian or others is a critical step for accurate determination of peak positions, intensities and widths, as well as the separation of overlapping peaks [57].

Considering the inherent chemical complexity of biological specimens, advanced multivariate data processing methods are usually involved in generating accurate Raman chemical images of cells or tissue samples. Unsupervised machine learning, such as principal component analysis (PCA) and clustering analysis, could manage data without labeled inputs. PCA processing extracts major variation patterns from high-dimensional spectral data, and contributes to the discrimination of the main components of the analyte, such as PC1, PC2, and PC3, representing the largest, second largest, and third largest principal component, separately [58], leading to the implementation of feature extraction and dimensionality reduction. For lipid analysis using Raman spectroscopy, PCA helps to reveal significant changes in chemical bonds or compositions in cells under different conditions. The analysis combining Raman spectroscopy with PCA was used to differentiate various immunophenotypes (CD45$^+$/CD38$^+$/CD138$^-$ and CD45$^-$/CD38$^+$/CD138$^+$) in multiple myeloma samples, and spectral features captured by PC1 and PC2 were primarily related to protein and lipid changes [59]. The algal cells under different durations of nitrogen stress were distinguished by PCA analysis, in which distinct clusters corresponding to different cell culture days were formed along PC1 (56%) and PC2 (26%), and β-carotene (1,521, 1,161, 1,152, and 1,001 cm^{-1}) and chlorophyll (1,534 and 1,182 cm^{-1}) were the major discriminating pigments [60]. Cluster analysis facilitates the identification of samples with similar spectral features [61], such as differentiating cancer cells and healthy cells [62]. Two clustering methods are frequently used in Raman spectroscopy, including k-means cluster analysis (KMCA) and hierarchical cluster analysis (HCA). KMCA was applied for multivariate analysis of SRS data by segmenting cellular images into distinct clusters corresponding to different biochemical regions, which successfully differentiated LD content and distribution in various cell models [63]. HCA clustered the characteristic spectral data of calcifications in breast tissue captured by CARS microscopy, for example, 1,490 and 1,464 cm^{-1} representing oxalate calcium associated with benign lesions and 961 cm^{-1} addressing phosphate calcium linked to malignant lesions [64]. The results are then mapped to form the spatial distribution of calcification types within the tissue thereby promoting the identification of potential pathological regions [64]. Supervised machine learning requires labeled data for training and prediction, such as partial least squares regression (PLS) and support vector machines (SVM). PLS is applied to the establishment of quantitative models for predicting analyte concentration and providing accurate chemical composition [53]. Raman imaging data processed by PLS regression models revealed that the increased unsaturated fatty acids (UFAs) but reduced glycoproteins could serve as biomarkers for monitoring cell transformation from human-induced pluripotent stem cells (iPSCs) into erythropoietin (EPO)-producing cells [65]. SVM maps spectral data into high-dimensional space and seeks the optimal hyperplane to discriminate different classes of multivariate data [66]. SVM distinguished Raman spectra data between radiation sensitive and resistant tumor cells, as radiation treatment caused obvious changes of lipids and collagen in sensitive tumors, while minimal changes were shown in resistant tumors [67]. Moreover, tumor radiation sensitivity was also predicted before treatment via SVM, contributing to

the creation of personalized treatments [67]. By combining unsupervised and supervised learning methods, valuable information could be effectively extracted from complex Raman spectral data. During the subtype identification of acute lymphoblastic leukemia (ALL) using Raman spectroscopy, PCA demonstrated the principally varied sources, PLS provided biochemical differences of cell types, and SVM optimized decision boundaries to obtain high specificity and sensitivity in the classification of ALL subtype [68].

5. Unraveling cellular lipid composition by Raman spectroscopy

The cellular lipidome mainly contains FAs, triglycerides (TGs), phospholipids, sphingolipids, glycolipids, and cholesterol. The Raman scattering cross-sections of lipids varied depending on the specific molecular structure and functional groups, particularly the long non-polar acyl chains, an integral part of the structure [69]. The signature bands in lipid Raman spectra are intrinsically linked to the hydrocarbon chains shown within the fingerprint region (500–2,000 cm^{-1}). Specifically, the bands spanning 1,500–1,400, 1,300–1,250, and 1,200–1,050 cm^{-1} are separately indicative of CH$_2$/CH$_3$ vibrations, CH$_2$ twisting vibrations, and C–C stretching vibrations [69]. In addition, the spectral domain between 2,900 and 2,800 cm^{-1} is also identified as a ubiquitous characteristic band among lipids, primarily attributed to C–H or =CH$_2$/CH$_3$ vibrations [69–71]. However, C–H stretching vibrations are also present in proteins such as CH$_3$ at 2,930 cm^{-1} and interference with protein signals should be judged carefully [70].

FAs, a class of long-chain carboxylic acids, fundamentally consist of an extended hydrocarbon chain terminated with a carboxyl group (–COOH). The length of the carbon chain and the degree of saturation (i.e., the number of C=C) determine the physical and chemical properties of FAs [72]. The Raman spectra of cellular FAs can be readily identified through distinctive spectral features. The most characteristic regions are approximately 1,500–1,400, 1,300, 1,180–1,060, and 890 cm^{-1} attributed separately to deformation vibrations of CH$_2$/CH$_3$, twisting vibrations of CH$_2$, stretching vibrations of C–C and C–O–O skeletal vibrations [69]. Notable distinctions between saturated fatty acids (SFAs) and UFAs are observed around 1,656 cm^{-1}, a pronounced band due to the C=C stretching vibrations, along with additional features related to =C–H stretching modes observed at approximately 3,015 cm^{-1} [70,73]. These spectral markers provide vital insights into the structural and functional effect of FAs within cellular contexts.

TGs primarily act as cellular energy reserves, mainly composed of a glycerol molecule esterified with three FA chains. Under the condition of increased energy demand, such as fasting or prolonged exercise, cellular TGs are broken down into glycerol and FAs for energy production and substance synthesis [74]. Each FA is connected to the glycerol's hydroxyl groups (–OH) via ester bonds. A peak around 1,100 cm^{-1} due to the C–O–C vibrations represents glycerol backbone, and a peak at approximately 1,740 cm^{-1} by C=O stretching vibrations indicates ester linkages [69,75]. The degree of unsaturation in TGs was positively associated with the characteristic Raman peak ratio I$_{1656/1444}$ [76].

Phospholipids are the primary lipids constituting the cellular membrane architecture, typically composed of a glycerol backbone, two FA chains, a phosphate group and a head group. The head group includes different types such as choline, ethanolamine, serine, and inositol. The spectral signature of phospholipids is profoundly influenced by the vibrations of the phosphatidyl moiety, with pronounced peaks typically observed within the 1,096–1,080 cm^{-1} range. Peaks corresponding to the P=O and P–O stretching vibrations within the phosphate group are common for many phospholipids and not unique to specific ones [69,77].

Moreover, the molecular vibrations of choline $N^+(CH_3)_3$ in phosphatidylcholine (PC) resonate 719 and 876 cm^{-1} [69,78]. The typical feature of the phosphatidylethanolamine (PE) spectrum is the 760 cm^{-1} band originating from the ethanolamine group [69]. In PS, Raman bands of serine residue are shown at 787, 733, 595, and 524 cm^{-1} [79]. For phosphatidylinositol (PI), the inositol residue is represented by Raman bands at 776, 576, 519 and 415 cm^{-1} [79]. Similarly to TGs, characteristic peaks associated with the glycerol backbone and ester bonds were also shown in phospholipids.

Sphingolipids contain a sphingosine backbone, an amide bond linked FA, and a head group that determines different types of sphingolipids [80]. Sphingomyelin (SM), a major type of sphingolipid, comprises the PC residue and ceramide backbone linking sphingosine and FA [79]. The primary Raman peak for SM is found at approximately 1,643 cm^{-1}, which is attributed to the amide I band, reflecting the amide linkage between the acyl chain and amino group of the sphingosine base [81]. Additionally, SM also exhibits choline bands, approximately located at 882 and 723 cm^{-1}, consistent with the characteristics of PC [69].

Glycolipids are composed of a lipid portion (usually sphingosine or glycerol) and one or more hydrophilic sugar heads linked by glycosidic bonds. They can be divided into glycosphingolipids and glycoglycerolipids according to the lipid moiety. Glycolipids play critical roles in cell recognition, signal transduction, and cell-cell interactions. The characteristic Raman spectra of glycolipids mainly arise from the sugar moiety, including peaks at 1,163 cm^{-1} representing asymmetric ring breathing of C–C and C–O–C glycosidic link, 1,126 cm^{-1} for symmetric ring breathing of C–C and C–O–C glycosidic link, 894 and 861 cm^{-1} for C–C and C–O–C 1,4 glycosidic link [82]. Furthermore, sphingoglycolipids also exhibit a distinct amide band around 1,660 cm^{-1} as shown in SM [79].

Cholesterol includes a steroidal nucleus consisting of four interconnected cycloalkane rings, conventionally designated as A, B, C, and D, which endow with molecular rigidity and planarity. As an indispensable component of cell membranes, cholesterol plays a crucial role in modulating membrane fluidity and rigidity. By reducing the mobility of phospholipids at high temperatures, cholesterol increases membrane rigidity [83]. Cholesterol also prevents phospholipids from packing too closely together at lower temperatures, thus preserving membrane fluidity [84]. One end of cholesterol is adorned with –OH which acts as a polar head group and facilitates the formation of hydrogen bonds with the polar heads of phospholipids, leading to the integrity and stability of the lipid bilayer [84]. This distinctive multicyclic configuration is an important character with specific Raman spectral signatures at approximately 704 and 548 cm^{-1} [26,79].

LDs are highly dynamic cellular organelles, which change their number, size and composition with the energy requirements in different cell types and even at different times within the same cells [85]. LDs mainly originate from the ER. In the inner leaflet of the ER membrane, neutral lipids such as TGs and cholesteryl esters (CEs) gradually accumulate and a lens-like structure is generated. Following continuous expansion, the structures dissociate from the ER membrane and finally form the individual LDs enveloped by a monolayer of phospholipids [86]. Raman profiles of LDs cover typical unsaturated TG signals, a prominent band at approximately 1,740 cm^{-1}, indicative of the carbonyl stretching vibration of ester bonds in TGs and CEs [71].

Raman spectroscopy plays an important role in delineating and discerning various lipid species, including but not limited to SFAs, UFAs, TGs, phospholipids, sphingolipids, glycolipids, and cholesterol. Qualitative analysis of lipids was carried out by the comparison of the sample's Raman spectra against reference spectra of known lipids. Based on the specific Raman peaks produced by different lipid classes, it is possible to simultaneously detect multiple lipid components in complex biological samples [69]. Xu et al. [87] first collected SRS spectra of several lipid standards as calibration references, and then successfully distinguished free cholesterol, saturated or unsaturated CE and TG in liver tissue sections through SRS spectral separation and linear least squares spectral decomposition algorithms. Moreover, the spatial distribution of these lipids within LDs was also exhibited via characteristic peak imaging [87]. On the other hand, quantitative analysis of lipids could be achieved by comparing the intensity of the characteristic peaks with those of known lipid standard solutions. SRS microscope captures lipid peaks at the specific Raman band 2,853 cm^{-1}, and the volume fraction of the specific lipids is proportionately measured after calibration and normalization processes [88]. Next, mass concentration is calculated according to the formula, mass concentration = volume fraction × density, in which density is a constant term for a specific lipid class, e.g. the density of dioleoylphosphatidylcholin (DOPC) is 1.0101 g/mL. In addition, the altered lipid contents under different physiological states were also revealed, such as Madin-Darby canine kidney (MDCK) cells undergoing cellular senescence and brain tissues of Alzheimer's disease model [88]. Here, the related characteristic peaks of cellular lipids are summarized in Table 1.

6. Analyzing lipid dynamic changes in LDs and cellular membranes using Raman imaging techniques

Raman imaging techniques are highly effective in identifying and mapping lipids within cells. Recently, microscopes integrated with Raman scattering such as SERS, CARS, SRS, and TERS have been developed [89]. By focusing a laser on each point and point-by-point scanning, Raman scattered light at each point is accordingly recorded. A 2D Raman image is produced by scanning across a single plane (typically the surface), while a 3D Raman image is generated by scanning at different depths and stacking these layers. Thus, this hyperspectral 2D or 3D imaging can visualize the spatial distribution of different lipids within cells, and this is useful for detailed analysis of lipid distribution, composition, and dynamic

Table 1
Feature peaks of lipids.

Biomolecule assignment	Molecular vibration	Raman band (cm^{-1})
Lipids	C–H stretching, CH_2/CH_3 vibrations	3,010–2,800
	CH_2/CH_3 vibrations	1,500–1,400
	CH_2 twisting	1,300–1,250
	C–C stretching	1,200–1,050
UFAs	=C––H stretching	3,015
	C=C stretching	1,656
TGs	C=O stretching	1,740
	C–O–C vibrations of glycerol backbone	1,100
FAs/TGs	(C–O–O) skeletal vibrations	890
Phospholipids	P=O and P–O stretching	1,096–1,080
	$N^+(CH_3)_3$ symmetric stretching of PC	876, 719
	Serine residue of PS	787, 733, 595, 524
	Inositol residue of PI	776, 576, 519, 415
	Ethanolamine of PE	760
Sphingolipids	Amide I	1,643
	$N^+(CH_3)_3$ symmetric stretching of SM	882, 723
Glycolipids	Amide I of sphingoglycolipids	1,660
	C–C, C–O–C glycosidic link, asymmetric ring breathing	1,163
	C–C, C–O–C glycosidic link, symmetric ring breathing	1,126
	C–C, C–O–C 1,4 glycosidic link	894, 861
Cholesterol/CEs	Cholesterol ring vibrations	704
	β($CH2$) in ringss	548
	C=O stretching of CEs	1,740

UFAs: unsaturated fatty acids; TGs: triglycerides; FAs: fatty acids; CEs: cholesteryl esters.

alterations. Additionally, time-lapse Raman imaging can monitor changes in the composition and distribution of lipids over time, providing deeper insights into dynamic biological processes such as lipid metabolism. Here, we mainly described the application of Raman imaging to analyze the main lipid structure LDs and plasma membranes.

Abnormal accumulation of LDs is associated with metabolic diseases and tumor development. Evidence is mounting that excess lipids stored in adipocytes and hepatocytes could cause insulin resistance and fatty liver disease [90], and the increase of LDs in tumor cells indicates enhanced invasion and metastasis capability [91]. Raman imaging is a sophisticated technique suitable for observing the biological features of LDs, including their size, abundance, localization and shape. Nan et al. [92] analyzed differentiated 3T3-L1 adipocytes using CARS imaging and found Raman shift at 2,845 cm^{-1} is associated with the high density of C−H bonds in LDs. Raman imagery of LDs closely resembled the patterns observed in Oil Red O staining, a comparative method to confirm the presence, size, and shape of LDs. The differentiation of human adipose-derived mesenchymal stem cells (hADMSCs) was also detected by Raman microscope, from nonexistent LDs to occurrence, and eventual formation of large LDs [46]. Compared to stromal vascular fraction (SVF)-derived adipocytes, primary adipocytes isolated from adipose tissue exhibit smoother and more uniform LD contours [71]. LDs in primary adipocytes have a higher degree of unsaturation which generally corresponds to rising flexibility, whereas those in SVF-derived mature cells have a higher saturation correlating to more rigidity [71]. The dynamics of LDs involving displacement, speed, travel length and directionality were obtained through 3D imaging at 2,884 cm^{-1} corresponding to lipid CH_2 vibrations using CARS microscopy [93]. In this process, a specialized MATLAB-based tool was established to analyze key parameters of LD trajectories. Moreover, the particle tracker plugin within ImageJ was integrated for tracking individual LD pathways. Recent research has been highlighted for direct observation of small-sized LDs and the entire dynamic process of LD biogenesis using SRS, in which real-time and 3D monitoring of cellular LD transport and interactions with other organelles such as ER and mitochondria was displayed [94].

Cell membranes are composed of phospholipid bilayer embedded with cholesterol and proteins. Dynamic microdomains within the cell membrane known as lipid rafts are enriched in cholesterol, sphingolipids, and saturated phospholipids, and play crucial roles in signal transduction, cell adhesion, and lipid/protein sorting [95]. Compared with optical imaging, Raman offers non-invasive, label-free imaging of the chemical structure of cell membranes. In 2011, Opilik et al. [96] utilized TERS for high-resolution imaging of lipid monolayers at the nanoscale with complete spectral information at each pixel, and recognized the first full-spectrum of phase-separated lipid structural domains, which improves our understanding of membrane structure and function. Recently, label-free TERS imaging has successfully visualized the molecular components, such as lipids, proteins, and cholesterol, within the cell membranes of human pancreatic cancer cells (BxPC-3) at a spatial resolution of approximately 2.5 nm [26]. This high spatial resolution provides great potential for revealing molecular characterization of complex biological samples and the distribution of biomolecules within different membrane domains, contributing to the identification of composition and dynamic alteration within cell membranes. Furthermore, TERS images were constructed without complex data processing but using the absolute intensity values of Raman marker bands, and thereby the efficiency was improved [26]. CARS is capable of displaying individual lipid bilayers and conducting quantitative analysis with high sensitivity. Potma et al. [97] employed CARS to study phase-separated lipid domains in free-standing bilayers from giant

unilamellar vesicles (GUVs), which eliminated geometrical constraints and provided a model closely resembling natural cell membranes. They selectively visualized phospholipid DOPC and 1,2-distearoyl-sn-glycero-3-phosphocholine (DSPC) and observed the distribution and phase separation of the membrane. The imaging results showed that DOPC and DSPC form distinct domains in the GUV membrane, with DOPC typically residing in the liquid-disordered phase and DSPC tending to form gel phases [97]. Following membrane disruption by NIR lasers, images of cell membranes were captured by CARS at the specific Raman shift of 2,840 cm^{-1} in living HeLa cells for the surveillance of the lipid distribution and membrane repair process [98]. Additionally, the molecular constituents in RBC membranes were detected in combination with silver nanostructures using SERS [99]. Similarly, individual membrane lipids and deoxyribonucleoside triphosphates (dNTPs) within live neuronal cells were also distinguished with high-resolution Raman imaging spectroscopy [100].

7. Application of Raman spectroscopy in lipid research of different cell types

After describing Raman spectroscopic characteristics of lipids and the foundational role of Raman imaging in LD and cell membrane, our focus now shifts to the application of Raman spectroscopy in diverse cell types including stem cells, adipocytes and cancer cells, for illustrating cellular phenotypes/genotypes, cell differentiation, population composition, apoptosis, cell cycle, and metabolic processes, especially lipid-related cellular functions [101−103].

7.1. Stem cell

Stem cells are undifferentiated cells with pluripotency and self-renewal capacity, which can be categorized into embryonic stem cells (ESCs) and somatic stem cells (SSCs) [104]. ESCs, derived from the inner cell mass of blastocyst-stage embryos, possess enormous proliferation and differentiation potential [105]. In contrast, SSCs found in specific tissues such as bone marrow, adipose tissue, skin, and brain, can differentiate into a limited cell type related to their derived tissues [104], such as hematopoietic stem cells (HSCs) differentiating into various blood cells [106]. With its non-destructive nature, Raman spectroscopy is useful for evaluating stem cell differentiation, quality and consistency [107].

Differentiation of stem cells is regulated by cellular energy production and biosynthetic pathways, and thereby this transformation could be observed by Raman through the identification of cellular nucleic acids, proteins, and lipids [108]. Differentiated human induced pluripotent stem cells (hiPSCs) significantly increased protein (1,660, 1,250, 1,030, and 1,003 cm^{-1}) and lipid (1,440 and 1,295 cm^{-1}) bands, but decreased nucleic acid bands (780 and 726 cm^{-1}) [108]. Raman imaging revealed the formation of adipocytes from adipose-derived stem cells (ADSCs) by LDs hallmark [46,48]. During this process, Raman microscopy imaging detected bright spots around the cell nucleus in the early stages (two days following induction), indicative of LD formation. Following the subsequent days, the morphology of the LDs became rounder and larger, and the intensities of lipid-related peaks were increased, especially at 3,013, 2,854, 2,727, 1,740, and 1,303 cm^{-1}, accompanied by a notable peak at 2,900 cm^{-1} [46]. Furthermore, the value of area calculation at the 2,900 cm^{-1} peak relative to that at 2,935 cm^{-1} could be used to quantify the stem cell differentiation process [46]. The hADMSCs were cultured on fibronectin-coated quartz substrate and induced to form adipocytes [109]. During the differentiation process, a 532 nm laser was focused on the live cells and Raman spectra were correspondingly collected, in which

the characteristic peaks in the range of 2,850–2,855 cm^{-1} representing the concentration of LDs were quantified to assess the adipogenic potential [109]. HSCs-derived neutrophils cultured on gold mirror-coated glass were immersed in phenol-free RPMI 1,640 medium for acquiring Raman spectral data, in which a significant increase of lipid components particularly choline headgroup (716 cm^{-1}) but a decrease of nucleic acid-associated signals was demonstrated, and partial least squares discriminant analysis (PLS-DA) model accurately predicted the differentiation states with a classification error rate of 11.3% [110].

The identification of stem cell types is also reported by Raman spectroscopy on the basis of obtained cellular lipid compositions [48]. Lipid constitutions in human embryonic stem cells (hESCs) and human mesenchymal stem cells (hMSCs) were reported as early as 2010 [111]. Compared with the induced pluripotent stem cells (iPSCs), mouse ESCs displayed higher spectral intensities at 1,650 and 1,260 cm^{-1} for C=C stretching in UFAs, such as arachidonic acid, docosahexaenoic acid and linoleic acid, but lower intensities at 1,445 cm^{-1} corresponding to saturated lipids [112]. This distinction indicates higher unsaturated lipids content in ESCs and reflects the dynamic changes of metabolism necessary for maintaining pluripotency. Simonović et al. [113] employed Raman spectroscopy to observe the differentiation of stem cells derived from various dental tissues, and found all of the cells displayed fingerprint regions within the 600–700 cm^{-1}, and characteristic lipid peaks at 1,650 and 1,440 cm^{-1} could be used to distinguish different types. Kukolj et al. [114] used Raman to identify bone marrow-derived mesenchymal stem cells (BM-MSCs) isolated from healthy child donors. Although BM-MSCs from various sources had similar Raman spectra, they could be distinct according to PCA analysis of lipids (1,450 cm^{-1} CH$_2$ scissoring in lipids and 1,310 cm^{-1} C–H deformation of saturated lipids), proteins, and nucleic acids. Harkness et al. [115] observed increased peak intensities at 1,300, 1,258, 1,196, and 1,158 cm^{-1} in abnormal MSCs and hESCs, in which peaks at 1,300 and 1,158 cm^{-1} were attributed to lipid-related structures.

7.2. Adipocytes

Adipocytes, differentiated from pluripotent stem cells, play a crucial role in the regulation of energy metabolism, endocrine and thermogenesis [116]. Mature adipocytes are categorized into three major types: white, brown and beige adipocytes [117]. White adipocytes possess large LDs to store energy and secrete hormones such as leptin and adiponectin to regulate systemic metabolism [117]. Brown adipocytes are characterized by smaller LDs and abundant mitochondria, with higher thermogenesis capacity depending on uncoupling protein 1 (UCP1) located in the mitochondrial inner membrane [118]. Beige adipocytes, a relatively newly discovered type, typically emerge within white adipose tissue and are induced by cold exposure or exercise stimuli. They possess multiple small LDs and numerous mitochondria and also dissipate energy as heat like brown adipocytes [118].

Raman spectroscopic techniques are employed to investigate characters of LDs in adipocytes. Differentiated adipocytes from OP9 bone marrow stromal cells under induced conditions (iOP9) exhibit larger LDs and higher unsaturation ratios, whereas spontaneously differentiated adipocytes (sOP9) display smaller LDs and lower unsaturation ratios [119]. However, there is no significant correlation between LD diameter and unsaturation ratio [119]. Time-lapse imaging of the LDs in 3T3-L1 derived adipocytes (at the C–H band) showed that micro-LDs (mLDs) initially originated from unspecific cytosol regions rather than from particularly adjacent large central LDs regions [120]. Furthermore, investigation on the chemical composition and physical state (acyl chain order) of individual LDs

exhibited that newly synthesized TGs were first stored in small LDs, not directly in the large LDs already present in adipocytes, and LDs expand by 'absorbing' lipid content of smaller 'donor' LDs. Importantly, lipid transfer between LDs spent several hours, indicating a finely regulated process rather than a rapid spontaneous fusion [121,122]. The saturation degree of LDs in FAs-stimulated adipocytes was reflected by the intensity ratio of 1,660 cm^{-1} band (C=C stretching) to 1,450 cm^{-1} band (CH$_2$ vibrations), and the unsaturation of LDs was increased by oleic acid (a monounsaturated fatty acid (MUFA)) and fish oil (a polyunsaturated fatty acid (PUFA)) but not stearic acid (a SFA) [123].

Utilizing deuterium labeling techniques, special chemical bonds are introduced in the cell-silent Raman window (1,800–2,600 cm^{-1}), allowing more precise tracking of the metabolic processes of lipid molecules [124]. Kumar et al. [29] pioneered the use of TERS technology for nanoscale chemical mapping of newly synthesized phospholipids in mouse pre-adipocytes pulsed with deuterated stearic acid sodium. These newly synthesized phospholipid molecules were likely to form elongated chain-like structures rather than aggregate into large clusters according to the Raman scattering peak of the carbon-deuterium (C–D) bond at 2,100 cm^{-1}. Another 9-h-long study was carried out to track the uptake of D-PA in brown adipocytes, and differences in CARS images were observed at 2,100, 1,741, and 1,655 cm^{-1} wavelengths, in which peaks at 2,100 cm^{-1} revealed the intracellular distribution of deuterated FAs and TG [125]. Subsequently, researchers assessed the ratios of C–D/C=O (indicating the content of deuterated FAs) and C=C/C=O (indicating the degree of lipid unsaturation) for each LD, and found that brown adipocytes inhibited the uptake of D-PA to maintain unsaturated lipid homeostasis [125].

The changes in lipid composition in adipocytes reflected by Raman spectroscopy facilitate illustrating the occurrence and progression of lipid metabolic diseases. The effects of high-glycemia (HG) on adipogenesis were observed by confocal Raman spectroscopy in human visceral preadipocytes [126]. The characteristic peaks (2,970, 2,934, 2,895, and 2,852 cm^{-1}) showed that HG not only accelerated adipogenesis but also altered the internal chemical composition of adipocytes including the significant increases of LDs number, suggesting that visceral fat may be a potential initial site for HG-induced metabolic disturbances [126]. Raman analysis of the adipocytes in perivascular adipose tissue (PVAT) from HFD-fed young or old mice showed that lipid unsaturation of adipocytes was reduced in old mice, while minimal changes were observed in young mice, indicating that PVAT was susceptible to HFD condition with increasing ages [127]. Preadipocytes and adipocytes treated by D-PA and tumor necrosis factor (TNF) could simulate the pathophysiological condition of HFD and chronic inflammation, respectively [128]. Preadipocytes sensitive to D-PA and TNF exhibited a significant accumulation of LDs but a decrease in lipid unsaturation. In mature adipocytes, the formation and expansion of LDs were also increased, but it was less pronounced than that in preadipocytes [128]. However, the number and composition of LDs in primary adipocytes remained largely unchanged [128]. These findings suggested that diet and inflammation play critical roles in obesity during the early stages of adipogenesis [128].

7.3. Cancer cell

Raman spectroscopy provides the possibility for non-invasive lipids analysis in cancer cells and thereby offers in-depth insights into tumor biology and metabolism. Raman spectroscopy combined with chemometric methods unveiled an increase in TG synthesis but a decrease of cholesterol in lung cancer cells (A549) compared with normal bronchial epithelial cells (BEpiC), and identified Raman lipid markers (2,936, 2,845, and 1,444 cm^{-1}) for cancer cells [129]. A

comparative Raman data between higher invasive M-4A4 cells and lower invasive NM-2C5 cells showed that the M-4A4 cell line possessed higher peak intensities at 1,657 and 1,263 cm^{-1} (vibrations of C=C and =CH) than those of NM-2C5 cells, indicating of the increased UFAs content in M-4A4 cells [130]. Moreover, the higher intensity at 1,657 and 1,263 cm^{-1} than the value of 1,440 cm^{-1} implied the presence of multiple double bonds due to polyunsaturated fatty acids (PUFAs). Therefore, the correlation between PUFA content and cancer metastasis was established. Similarly, non-metastatic cancer cells 67NR were successfully distinguished from metastatic cancer cells FARN, 4T07, and 4T1 cells using a machine-learning model based on spectral data of collagen and lipids [55].

On the other hand, the genotypes of cancer cells could be determined by Raman imaging analysis. Raman spectroscopy was employed to differentiate cyclin-dependent kinase 6 (CDK6) gene knockout (KO) HeLa cells from wild-type (WT) cells [70]. SFAs content in KO cells was increased compared with that in WT cells. The band ratios of SFAs/UFAs in the Raman spectrum (I_{1301}/I_{1444}, I_{1656}/I_{2852}, I_{1656}/I_{3013}, I_{2852}/I_{3013}, and I_{2930}/I_{3013}, etc.) were characterized as Raman spectroscopic markers for discriminating WT and KO cells [70]. Additionally, the accumulated LDs were found in prominin-1 positive melanoma cells according to CH$_2$ stretching vibration at 2,845 cm^{-1} shown by CARS, while minimal LDs were illustrated in prominin-1 knockdown cells, suggesting that prominin-1 promoted intracellular LD accumulation and regulated cellular lipid metabolism [131]. The role of CUB-domain containing protein 1 (CDCP1) on lipid metabolism was investigated by CARS and two-photon excited fluorescence (TPEF) microscopy, in which CDCP1 could reduce cytosolic LD abundance but increase FA oxidation, and thereby drives triple-negative breast cancer (TNBC) metastasis [132]. The Von Hippel-Lindau (VHL) gene is a tumor suppressor that facilitates the degradation of hypoxia-inducible factor 1α (HIF1α), whereas mutations of VHL impaired HIF1α degradation, and consequently cause the accumulation of HIF1α and tumor development [133]. Clear cell renal cell carcinoma (ccRCC) samples with or without VHL mutation were analyzed by Raman. VHL-mutant tumor cells increased CE-related peaks at 1,742 cm^{-1}, 1,442 cm^{-1}, and 702 cm^{-1} [134], and following the reintroduction of wild-type VHL gene, the number of LDs and CE levels were correspondingly reduced [134].

Raman spectroscopy technology could disclose the alteration of lipid metabolism related to cancer development, progression, and pharmacological interventions [135,136]. Growth suppression of prostate cancer cells (PC3) by X-ray radiation could be attributed to the altered intensity of lipids rather than the composition of LDs [137]. Compared with human epidermal growth factor receptor 2 (HER2)-negative breast cancer cells MCF-10A, HER2-positive BT474 and MCF-10A cells exhibited significant upregulation of lipid content, as evidenced by the increased Raman peaks at 1,660, 1,338, and 1,304 cm^{-1} [138]. BT474-LR cells with resistance against lapatinib, an oral dual tyrosine kinase inhibitor, possessed a higher phospholipid content than that of sensitive BT474 cells, which were specifically marked by the enhanced Raman peaks at 1,657, 1,333, and 1,307 cm^{-1} [138]. Jamieson et al. [139] evaluated the effects of lipid-targeted drugs on PC3 cancer cells by comparing spectral bands from 2,800 to 3,100 cm^{-1}. The altered lipid content of hormone-sensitive breast cancer cells and prostate cancer cell were particularly manifested in LDs and SFAs amount by imaging lipid distribution and analyzing Raman data (2,800−3,015 and 830−1,800 cm^{-1}) [140].

7.4. Hepatocytes, oocytes, endothelial and muscle cells with the potential for lipid storage

Raman spectroscopy demonstrates extensive applicability and flexibility in cell lipid studies, particularly in cells with the potential

for lipid storage under specific conditions. Lipid storage is a crucial cellular process with diverse implications across different cell types.

In hepatocytes, LDs can supply energy and maintain blood lipid balance [141]. However, abnormal accumulation of LDs may lead to metabolic diseases such as non-alcoholic fatty liver disease (NAFLD) and obesity [142]. Raman imaging successfully exhibited the accumulation of LDs, as well as their molecular characteristics in hepatocytes [143]. Very low-density lipoprotein (VLDL) lipolysis products could induce rapid accumulation of LDs and the increase of UFAs in primary hepatocytes by CARS analysis [144]. Co-stimulation with SFAs such as palmitic acid and UFAs such as oleic acid and 13-hydroxyoctadecadienoic acid (13-HODE), increased cellular saturated lipid content and saturation degree in the cores of LDs, meanwhile, more esterified UFAs were synthesized to neutralize the toxicity of SFAs [144]. Raman spectroscopy data of LDs in FAs-treated HepG2 cells demonstrated that high concentrations of SFAs (palmitic and stearic acids) led to lower amounts of LDs and induction of cellular apoptosis [145], whereas oleic and linoleic acids stimulation resulted in higher accumulation of LDs, and cell death could be particularly triggered by linoleic acid but not oleic acid. Additionally, FA chains of linoleic acid entering the cells were changed into the form of oleic acid, suggesting that the mechanism by which linoleic acid induces hepatocyte death might differ from that of SFAs [145]. Ma et al. [146] assessed the feasibility of Raman spectroscopy to identify proliferating human hepatocytes. Using representative Raman biomarkers including phenylalanine (1,003 cm^{-1}), hydroxyproline (1,206 cm^{-1}), and lipid-related (1,744, 1,440, 1,300, and 1,080 cm^{-1}) and a two-layer machine-learning model, proliferating human hepatocytes were successfully discriminated from primary human hepatocytes (PHHs).

In oocytes, the presence of LDs plays a pivotal role in regulating cellular maturation and development, providing necessary energy and structural components for early embryogenesis [147]. Recent studies have also found a positive correlation between the number of LDs and the length of embryo diapause (ED) [148]. Raman spectroscopy is an indispensable technique for evaluating the quality of oocytes and the viability of embryos before implantation in mammals. Specifically, the ratio of peak intensities at phenylalanine-associated 1,605 cm^{-1} to lipid C−H deformation-related 1,447 cm^{-1} indicated the protein-to-lipid ratio in oocytes, and a higher ratio correlated with high-quality development [149]. Lipid phase transitions in oocytes could be observed by Raman spectroscopy, contributing to the improvement of cryopreservation techniques. Okotrub's work on *in situ* label-free characterization of lipid phase transitions in frozen oocytes and embryos demonstrated the temperature-dependent evolution of LD phase states for the first time [150]. Their subsequent study with deuterated lipids showed lipid phase separation in cryopreserved oocytes. In oocytes supplemented with stearic acid, cellular saturated lipids originally formed an ordered phase at the LD periphery, and upon warming post-cooling, a fraction of saturated lipids still remained in the ordered state, while mono-/poly-unsaturated lipids were redistributed to the LD core, accompanied with monounsaturated lipids transiting to the ordered state below −10 °C [151]. Their latest research indicated that cooling may irreversibly alter the lipid phase state in porcine oocytes [152].

In endothelial cells, LDs can buffer lipotoxicity and provide energy for the cells themselves and other parenchymal cells [153]. However, excessive lipid storage can impair vascular health, leading to atherosclerosis and hypertension [154]. Confocal Raman high-resolution imaging technology was used to observe LDs formation within endothelial cells in three dimensions [155] and the process of LDs formation stimulated by PUFAs [156,157], and LDs

formation in endothelial cells was confirmed according to characteristic =C–D stretching mode bands (2,200–2,300 cm^{-1}) of deuterium-labeled arachidonic acid (AA-d8) [156]. By Solver plugin, the proportion of oleic acid and arachidonic acid in LDs was successfully estimated in which the composition of oleic acid LDs accounting for 80.6–91.3%, while arachidonic acid ranges from 8.7% to 19.4% in the cultured endothelial cells and *ex vivo* vascular endothelial cells. It suggested that endothelial cells are capable of absorbing exogenous oleic acid from the medium as well as releasing endogenous arachidonic acid [157]. Thus, Raman technology could be helpful for the surveillance of the occurrence and progression of various vascular diseases [158]. Radwan et al. [159,160] investigated the potential of (3S,3′S)-astaxanthin (AXT) as a novel Raman probe for the specific resonant Raman scattering spectrum at 1,520, 1,159, and 1,009 cm^{-1}, which allowed for clearer detection of lipid changes in endothelial cells across various vascular beds, including the aorta, brain, and heart. AXT encapsulation with liposomes significantly enhanced its uptake in endothelial cells, and free or encapsulated AXT not only decreased lipid unsaturation and LD numbers but also possessed a certain anti-inflammatory capacity in TNF-α-treated endothelial cells [160].

In muscle cells, LDs act as energy reservoirs during exercise, while abnormal lipid accumulation in muscle cells disrupts energy metabolism and is associated with insulin resistance and muscular dystrophies [161]. The lipid characteristics of muscle cells from Raman analysis were also summarized here. The alterations of saturation and length of triacylglycerol acyl chain within the LDs in muscle cells were minimal [162], but the size and subcellular localization of LDs were significantly distinctive between athletes and type 2 diabetes patients. Athletes stored most of their lipids in numerous and normally sized LDs in the intramyofibrillar (IMF) area of type I muscle fibers, while individuals with type 2 diabetes stored most of their lipids in fewer, but larger LDs predominantly in the subsarcolemmal (SS) area of type II muscle fibers [163]. Notably, in type 2 diabetic patients, larger LDs exhibited longer acyl chains than normally size LDs, suggesting a possible association of larger LDs and SS area with reduced insulin sensitivity. Thus, these findings offer novel insights into the determination of insulin sensitivity by comparing LDs of muscle cells [162].

8. Future application of Raman spectroscopy in cellular lipids

Advanced and effective approaches targeting the hardware and software of Raman microscopy could substantially improve systemic sensitivity, resolution, and portability. The novel nano-materials as well as composites used as SERS substrates will facilitate the detection of low-concentration molecules by capturing stable and increased signals [164]. Optimizing probe materials and surface coatings, along with refining probe shapes and geometric structures, could improve TERS signals [165]. Integrating super-resolution microscopy (such as stimulated emission depletion microscopy (STED), structured illumination microscopy (SIM), and photoactivated localization microscopy (PALM)/stochastic optical reconstruction microscopy (STORM)) with Raman could surpass the limit light diffraction and fulfill nanometer-level resolution [166]. Additionally, a convenient and user-friendly operation system is important for the widespread use of Raman in clinical diagnosis and treatment, such as the application of digital micromirror devices, micro-spectrometers, micro-lasers, as well as spectral preprocessing software and modular design.

Raman multimodal imaging is a promising technology that combines Raman spectroscopy with varied methods to obtain comprehensive information about analytes and overcomes the limitations of standalone Raman technology in terms of sensitivity, resolution, and specific molecular detection. By integrating with

fluorescence microscopy, Raman spectroscopy not only provides the chemical composition information without complex sample preparation, but also allows the capture of high-resolution cellular structure images, which enables more accurate identification of lipid components in specific cell substructures [68]. Additionally, fluorescence microscopy could help identify the source of fluorescent signals and localize Raman imaging in specific regions, resulting in the effective reduction of fluorescent interference with Raman signals. In metabolic research, the integration of Raman spectroscopy with MS broke through the limitations of Raman spectroscopy in lipid identification, and thereby the composition and distribution of intracellular lipids were clearly identified [167]. Integration of Raman technology with super-resolution microscopy and time-resolved technologies will increase its signal intensities and temporal resolution for real-time and multidimensional monitoring of cellular dynamics alterations.

A comprehensive Raman database will be produced by integrating it with other omics data. Recently, several Raman spectroscopy databases have been established, such as "A SERS Database of 63 Metabolites" [168] and "A Raman Database of 161 Inorganic Compounds" [169]. These databases typically focused on a single range of chemical compounds, often contained limited spectra information for biological samples and lacked interoperability with other databases. Therefore, future comprehensive databases could be built to store and manage extensive datasets derived from Raman spectroscopy. For cellular lipidomics research, besides fundamental Raman spectra of single lipid standards, the database should also include spectra signals from various cell types and cells under different physiological conditions. Additionally, the correlation of Raman spectral data with lipidomics, genomics, and transcriptomics will provide a more convenient exploration of cellular metabolic processes and molecular mechanisms, which is particularly crucial for studying metabolism-related diseases.

The development of artificial intelligence (AI) not only addresses the limitations of traditional Raman spectroscopy in data processing, signal-to-noise ratio and dynamic experimental adjustments, but also expands its application in clinical disease diagnosis and treatment. AI algorithms can significantly enhance the efficiency of Raman spectral data analysis, especially in handling large-scale, high-throughput datasets. Machine learning algorithms have already been successfully used to identify patterns in disease-related Raman spectra [170]. The generation of self-driven Raman spectroscopy offers the possibility for automated sample preparation, data acquisition and analysis, contributing to the reduction of human error and improvement of experimental efficiency. The autoregulation of parameters such as laser intensity and exposure time by AI-enhanced optimal signal quality in the dynamic process of cellular metabolism. AI models trained by high-throughput Raman spectral data are expected to become valuable tools for the diagnosis and treatment of clinical diseases. A rigorous monitoring system for the spectra of metabolites in blood and urine samples is useful for the early detection of metabolic diseases like diabetes and cardiovascular disorders. On the other hand, AI analysis of Raman spectral signals together with genomic and metabolic data from the same patient, will provide personalized diagnosis and treatment recommendations for an increase of therapeutic effects.

9. Clinical implementation of Raman spectroscopy

Raman spectroscopy could also be used to diagnose diseases, such as cardiovascular diseases, NAFLD, lung cancer, breast carcinoma and skin tumor [171]. A novel technique combined with fiber-optic Raman spectroscopy and spectral modeling was employed in the rapid characterization of lipid unsaturation and

carotenoid content in the PVAT surrounding the internal mammary artery (IMA) [172]. The phenotype of PVAT was closely related to the Canadian Cardiovascular Society (CCS) Angina Grading Scale, and it could provide a quick assessment for grafted IMAs in patients undergoing coronary artery bypass surgery [172]. The image-guided Raman spectroscopic probe-tracking system based on white light/fluorescence images precisely delineated tumor margins from healthy tissues *in vitro* and *in vivo*, contributing to the complete removal of tumor tissues while the preservation of healthy tissue as much as possible [173]. The integration of portable Raman spectroscopic devices with dermoscopy and computer-aided systems permitted the simultaneous acquisition of biochemical and morphological information on skin tissues for the accurate diagnosis of skin tumor [174]. However, the inherently weak Raman signals pose challenges to rapidly and non-invasively acquire high-quality signals in clinical samples, especially *in vivo* [171], and provide the requirement for high-power laser sources and highly sensitive detectors which consequently increases equipment costs. The optical fibers in Raman systems not only articulate light delivery but also meet medical requirements for different clinical targets [175]. The variations in sample preparation procedures, such as fixation methods and thickness of tissue section, could lead to significant differences in spectral signals and potentially compromise diagnostic consistency. Therefore, both the complex chemical composition in biological samples and technical consistency across different laboratories remain great challenges for the clinical implementation of Raman.

10. Conclusions

The integration of Raman spectroscopy with different imaging instruments offers valuable insights into cellular lipid metabolism in a non-invasive approach, and the advanced statistical techniques and machine learning algorithms facilitate the interpretation of complex Raman spectral data. Nevertheless, the limitations of Raman are still existent. The accuracy in identifying lipid species within complex tissue matrices is inherently limited, particularly for lipids at low concentrations or heterogeneously dispersed and culminated in attenuated Raman signals. Considering the limitations of laser wavelength and weak signals from small structures, most conventional Raman spectroscopy methods are typically only suitable for revealing lipid compositions in larger structures such as LDs and cell membranes. Advanced techniques such as SERS, TERS, and SRS enhance Raman spatial resolution at the nanoscale and make it possible for the discrimination of smaller organelles like mitochondria, lysosomes and ER. However, precise positioning, elimination of background interference and high operational skills still are challenges for further in-depth study of intracellular organelles and their dynamic changes. Furthermore, despite the support of signal deconvolution methods and machine learning algorithms, quantitative analysis of lipids still needs great exploration.

CRediT authorship contribution statement

Yixuan Zhou: Writing − review & editing, Writing − original draft, Data curation, Conceptualization. **Yuelin Xu:** Writing − review & editing, Writing − original draft, Data curation. **Xiaoli Hou:** Writing − review & editing, Writing − original draft, Visualization. **Daozong Xia:** Writing − review & editing, Writing − original draft, Visualization, Conceptualization.

Declaration of competing interest

The authors declare that there are no conflicts of interest.

References

[1] R.A. DeBose-Boyd, Significance and regulation of lipid metabolism, Semin. Cell Dev. Biol. 81 (2018), 97.

[2] M.F. Lanfranco, C.A. Ng, G.W. Rebeck, ApoE lipidation as a therapeutic target in Alzheimer's disease, Int. J. Mol. Sci. 21 (2020), 6336.

[3] X. Guo, T. Zhang, L. Shi, et al., The relationship between lipid phytochemicals, obesity and its related chronic diseases, Food Funct. 9 (2018) 6048−6062.

[4] Z. Wu, G.I. Bagarolo, S. Thoröe-Boveleth, et al., "Lipidomics": Mass spectrometric and chemometric analyses of lipids, Adv. Drug Deliv. Rev. 159 (2020) 294−307.

[5] M. Lange, M. Fedorova, Evaluation of lipid quantification accuracy using HILIC and RPLC MS on the example of NIST® SRM® 1950 metabolites in human plasma, Anal. Bioanal. Chem. 412 (2020) 3573−3584.

[6] C. Giovagnoni, S.M. Crivelli, M. Losen, et al., Immunofluorescence labeling of lipid-binding proteins CERTs to monitor lipid raft dynamics, Methods Mol. Biol. 2187 (2021) 327−335.

[7] H. Appelqvist, K. Stranius, K. Börjesson, et al., Specific imaging of intracellular lipid droplets using a benzothiadiazole derivative with solvatochromic properties, Bioconjug. Chem. 28 (2017) 1363−1370.

[8] N. Schieda, C.B. van der Pol, B. Moosavi, et al., Intracellular lipid in papillary renal cell carcinoma (pRCC): T2 weighted (T2W) MRI and pathologic correlation, Eur. Radiol. 25 (2015) 2134−2142.

[9] J.C. Matuszczyk, G. Zijlstra, D. Ede, et al., Raman spectroscopy provides valuable process insights for cell-derived and cellular products, Curr. Opin. Biotechnol. 81 (2023), 102937.

[10] U.P. Agarwal, 1064 nm FT-Raman spectroscopy for investigations of plant cell walls and other biomass materials, Front. Plant Sci. 5 (2014), 490.

[11] F. Gao, L. Xu, Y. Zhang, et al., Analytical Raman spectroscopic study for discriminant analysis of different animal-derived feedstuff: Understanding the high correlation between Raman spectroscopy and lipid characteristics, Food Chem. 240 (2018) 989−996.

[12] F.C.C. Oliveira, C.R.R. Brandão, H.F. Ramalho, et al., Adulteration of diesel/biodiesel blends by vegetable oil as determined by Fourier transform (FT) near infrared spectrometry and FT-Raman spectroscopy, Anal. Chim. Acta 587 (2007) 194−199.

[13] B. Tołpa, W. Paja, E. Trojnar, et al., FT-Raman spectra in combination with machine learning and multivariate analyses as a diagnostic tool in brain tumors, Nanomedicine 57 (2024), 102737.

[14] M. Kluz-Barłowska, T. Kluz, W. Paja, et al., FT-Raman and FTIR spectroscopy as a tools showing marker of platinum-resistant phenomena in women suffering from ovarian cancer, Sci. Rep. 14 (2024), 11025.

[15] B. Schrader, G. Baranović, S. Keller, et al., Micro and two-dimensional NIR FT Raman spectroscopy, Fresenius' J. Anal. Chem. 349 (1994) 4−10.

[16] L. Kelbauskas, R. Shetty, B. Cao, et al., Optical computed tomography for spatially isotropic four-dimensional imaging of live single cells, Sci. Adv. 3 (2017), e1602580.

[17] G.W. Auner, S.K. Koya, C. Huang, et al., Applications of Raman spectroscopy in cancer diagnosis, Cancer Metastasis Rev. 37 (2018) 691−717.

[18] C. Krafft, J. Popp, The many facets of Raman spectroscopy for biomedical analysis, Anal. Bioanal. Chem. 407 (2015) 699−717.

[19] G. Qi, J. Wang, K. Ma, et al., Label-free single-particle surface-enhanced Raman spectroscopy detection of phosphatidylserine externalization on cell membranes with multifunctional micron-nano composite probes, Anal. Chem. 93 (2021) 2183−2190.

[20] D. Zhu, Z. Wang, S. Zong, et al., Investigating the intracellular behaviors of liposomal nanohybrids *via* SERS: Insights into the influence of metal nanoparticles, Theranostics 8 (2018) 941−954.

[21] X.S. Zheng, I.J. Jahn, K. Weber, et al., Label-free SERS in biological and biomedical applications: Recent progress, current challenges and opportunities, Spectrochim. Acta A Mol. Biomol. Spectrosc. 197 (2018) 56−77.

[22] A. Gall, A.A. Pascal, B. Robert, Vibrational techniques applied to photosynthesis: Resonance Raman and fluorescence line-narrowing, Biochim. Biophys. Acta 1847 (2015) 12−18.

[23] M. Ishigaki, P. Meksiarun, Y. Kitahama, et al., Unveiling the aggregation of lycopene *in vitro* and *in vivo*: UV-vis, resonance Raman, and Raman imaging studies, J. Phys. Chem. B 121 (2017) 8046−8057.

[24] U. Blume-Peytavi, A. Rolland, M.E. Darvin, et al., Cutaneous lycopene and beta-carotene levels measured by resonance Raman spectroscopy: High reliability and sensitivity to oral lactolycopene deprivation and supplementation, Eur. J. Pharm. Biopharm. 73 (2009) 187−194.

[25] R.E. Kast, S.C. Tucker, K. Killian, et al., Emerging technology: Applications of Raman spectroscopy for prostate cancer, Cancer Metastasis Rev. 33 (2014) 673−693.

[26] D. Mrđenović, W. Ge, N. Kumar, et al., Nanoscale chemical imaging of human cell membranes using tip-enhanced Raman spectroscopy, Angew. Chem. Int.

Ed 61 (2022), e202210288.

[27] P. Verma, Tip-enhanced Raman spectroscopy: Technique and recent advances, Chem. Rev. 117 (2017) 6447–6466.

[28] R. Böhme, M. Mkandawire, U. Krause-Buchholz, et al., Characterizing cytochrome c states: TERS studies of whole mitochondria, Chem. Commun. (Camb) 47 (2011) 11453–11455.

[29] N. Kumar, M.M. Drozdz, H. Jiang, et al., Nanoscale mapping of newly-synthesised phospholipid molecules in a biological cell using tip-enhanced Raman spectroscopy, Chem. Commun. (Camb) 53 (2017) 2451–2454.

[30] T. Stepanenko, K. Sofińska, N. Wilkosz, et al., Surface-enhanced Raman scattering (SERS) and tip-enhanced Raman scattering (TERS) in label-free characterization of erythrocyte membranes and extracellular vesicles at the nano-scale and molecular level, Analyst 149 (2024) 778–788.

[31] Y. Pandey, N. Kumar, G. Goubert, et al., Nanoscale chemical imaging of supported lipid monolayers using tip-enhanced Raman spectroscopy, Angew. Chem. Int. Ed 60 (2021) 19041–19046.

[32] A. Folick, W. Min, M.C. Wang, Label-free imaging of lipid dynamics using Coherent Anti-stokes Raman Scattering (CARS) and Stimulated Raman Scattering (SRS) microscopy, Curr. Opin. Genet. Dev. 21 (2011) 585–590.

[33] C. Di Napoli, I. Pope, F. Masia, et al., Hyperspectral and differential CARS microscopy for quantitative chemical imaging in human adipocytes, Biomed. Opt. Express 5 (2014) 1378–1390.

[34] J. Saarinen, E. Sözeri, S.J. Fraser-Miller, et al., Insights into Caco-2 cell culture structure using coherent anti-Stokes Raman scattering (CARS) microscopy, Int. J. Pharm. 523 (2017) 270–280.

[35] L. Guo, J. Huang, Y. Chen, et al., Fiber-enhanced stimulated Raman scattering and sensitive detection of dilute solutions, Biosensors (Basel) 12 (2022), 243.

[36] M.C. Wang, W. Min, C.W. Freudiger, et al., RNAi screening for fat regulatory genes with SRS microscopy, Nat. Methods 8 (2011) 135–138.

[37] C. Cao, D. Zhou, T. Chen, et al., Label-free digital quantification of lipid droplets in single cells by stimulated Raman microscopy on a microfluidic platform, Anal. Chem. 88 (2016) 4931–4939.

[38] A. Borek-Dorosz, A. Pieczara, K. Czamara, et al., What is the ability of inflamed endothelium to uptake exogenous saturated fatty acids? A proof-of-concept study using spontaneous Raman, SRS and CARS microscopy, Cell. Mol. Life Sci. 79 (2022), 593.

[39] R. Smith, K.L. Wright, L. Ashton, Raman spectroscopy: An evolving technique for live cell studies, Analyst 141 (2016) 3590–3600.

[40] J.W. Chan, D.S. Taylor, D.L. Thompson, The effect of cell fixation on the discrimination of normal and leukemia cells with laser tweezers Raman spectroscopy, Biopolymers 91 (2009) 132–139.

[41] S.M. Levchenko, X. Peng, L. Liu, et al., The impact of cell fixation on coherent anti-stokes Raman scattering signal intensity in neuronal and glial cell lines, J. Biophotonics 12 (2019), e201800203.

[42] C. Jüngst, M. Klein, A. Zumbusch, Long-term live cell microscopy studies of lipid droplet fusion dynamics in adipocytes, J. Lipid Res. 54 (2013) 3419–3429.

[43] C. Zhang, S.A. Boppart, Tracking the formation and degradation of fatty-acid-accumulated mitochondria using label-free chemical imaging, Sci. Rep. 11 (2021), 6671.

[44] A. Zoladek, F. Pascut, P. Patel, et al., Development of Raman Imaging System for time-course imaging of single living cells, Spectroscopy 24 (2010) 131–136.

[45] E. Aboualizadeh, E.C. Mattson, C.L. O'Hara, et al., Cold shock induces apoptosis of dorsal root ganglion neurons plated on infrared windows, Analyst 140 (2015) 4046–4056.

[46] I.R. Suhito, Y. Han, J. Min, et al., In situ label-free monitoring of human adipose-derived mesenchymal stem cell differentiation into multiple lineages, Biomaterials 154 (2018) 223–233.

[47] M. Gargotti, E. Efeoglu, H.J. Byrne, et al., Raman spectroscopy detects biochemical changes due to different cell culture environments in live cells in vitro, Anal. Bioanal. Chem. 410 (2018) 7537–7550.

[48] Y. Tan, S.O. Konorov, H.G. Schulze, et al., Comparative study using Raman microspectroscopy reveals spectral signatures of human induced pluripotent cells more closely resemble those from human embryonic stem cells than those from differentiated cells, Analyst 137 (2012) 4509–4515.

[49] L. Yang, J. Motohisa, J. Takeda, et al., Selective-area growth of hexagonal nanopillars with single InGaAs/GaAs quantum wells on GaAs(111)B substrate and their temperature-dependent photoluminescence, Nanotechnology 18 (2007), 105302.

[50] O. Ryabchykov, J. Popp, T. Bocklitz, Fusion of MALDI spectrometric imaging and Raman spectroscopic data for the analysis of biological samples, Front. Chem. 6 (2018), 257.

[51] V. Avilkina, D. Leterme, G. Falgayrac, et al., Severity level and duration of energy deficit in mice affect bone phenotype and bone marrow stromal cell differentiation capacity, Front. Endocrinol. (Lausanne) 13 (2022), 880503.

[52] M.J. Hackett, J.B. Aitken, F. El-Assaad, et al., Mechanisms of murine cerebral malaria: Multimodal imaging of altered cerebral metabolism and protein oxidation at hemorrhage sites, Sci. Adv. 1 (2015), e1500911.

[53] J. Marzi, E. Fuhrmann, E. Brauchle, et al., Non-invasive three-dimensional cell analysis in bioinks by Raman imaging, ACS Appl. Mater. Interfaces 14 (2022) 30455–30465.

[54] H. Salehi, A. Ramoji, S. Mougari, et al., Specific intracellular signature of SARS-CoV-2 infection using confocal Raman microscopy, Commun. Chem. 5 (2022), 85.

[55] S.K. Paidi, J.R. Troncoso, M.G. Harper, et al., Raman spectroscopy reveals phenotype switches in breast cancer metastasis, Theranostics 12 (2022) 5351–5363.

[56] H. Chi, S. Hu, D. Lin, Development of an automated Raman system and use of principal component analysis to classify real and counterfeit liquors, RSC Adv. 13 (2023) 33288–33293.

[57] Y. Jin, H. Tian, Z. Gao, et al., Oil content analysis of corn seeds using a hand-held Raman spectrometer and spectral peak decomposition algorithm, Front. Plant Sci. 14 (2023), 1174747.

[58] Anu, A. Srivastava, M.S. Khan, Principle component analysis for nonlinear optical properties of thiophene-based metal complexes, J. Mol. Model. 27 (2021), 340.

[59] M. Bonsignore, S. Trusso, C. De Pasquale, et al., A multivariate analysis of Multiple Myeloma subtype plasma cells, Spectrochim. Acta A Mol. Biomol. Spectrosc. 258 (2021), 119813.

[60] Y. Shao, H. Fang, H. Zhou, et al., Detection and imaging of lipids of Scenedesmus obliquus based on confocal Raman microspectroscopy, Biotechnol. Biofuels 10 (2017), 300.

[61] H. Xin, J. Zhang, C. Yang, et al., Direct detection of inhomogeneity in CVD-grown 2D TMD materials via K-means clustering Raman analysis, Nanomaterials (Basel) 12 (2022), 414.

[62] I.W. Schie, T. Huser, Methods and applications of Raman microspectroscopy to single-cell studies, Appl. Spectrosc. 67 (2013) 813–828.

[63] E.W. Hislop, W.J. Tipping, K. Faulds, et al., Label-free imaging of lipid droplets in prostate cells using stimulated Raman scattering microscopy and multivariate analysis, Anal. Chem. 94 (2022) 8899–8908.

[64] G.I. Petrov, R. Arora, V.V. Yakovlev, Coherent anti-Stokes Raman scattering imaging of microcalcifications associated with breast cancer, Analyst 146 (2021) 1253–1259.

[65] M. Ishigaki, H. Hitomi, Y. Ozaki, et al., Exposing intracellular molecular changes during the differentiation of human-induced pluripotent stem cells into erythropoietin-producing cells using Raman spectroscopy and imaging, Sci. Rep. 12 (2022), 20454.

[66] N. Su, S. Weng, L. Wang, et al., Reflectance spectroscopy with multivariate methods for non-destructive discrimination of edible oil adulteration, Biosensors (Basel) 11 (2021), 492.

[67] S.K. Paidi, P.M. Diaz, S. Dadgar, et al., Label-free Raman spectroscopy reveals signatures of radiation resistance in the tumor microenvironment, Cancer Res. 79 (2019) 2054–2064.

[68] A. Adamczyk, A.M. Nowakowska, J. Jakubowska, et al., Raman classification of selected subtypes of acute lymphoblastic leukemia (ALL), Analyst 149 (2024) 571–581.

[69] K. Czamara, K. Majzner, M.Z. Pacia, et al., Raman spectroscopy of lipids: A review, J. Raman Spectrosc. 46 (2015) 4–20.

[70] Y. Xu, X. Hou, Q. Zhu, et al., Phenotype identification of HeLa cells knockout CDK6 gene based on label-free Raman imaging, Anal. Chem. 94 (2022) 8890–8898.

[71] E. Stanek, M.Z. Pacia, A. Kaczor, et al., The distinct phenotype of primary adipocytes and adipocytes derived from stem cells of white adipose tissue as assessed by Raman and fluorescence imaging, Cell. Mol. Life Sci. 79 (2022), 383.

[72] N. Dahdah, A. Gonzalez-Franquesa, S. Samino, et al., Effects of lifestyle intervention in tissue-specific lipidomic profile of formerly obese mice, Int. J. Mol. Sci. 22 (2021), 3694.

[73] R. Basson, C. Lima, H. Muhamadali, et al., Assessment of transdermal delivery of topical compounds in skin scarring using a novel combined approach of Raman spectroscopy and high-performance liquid chromatography, Adv. Wound Care (New Rochelle) 10 (2021) 1–12.

[74] K.J. Lee, G.E. Ji, Free-fatty-acid-regulating effects of fermented red ginseng are mediated by hormones and by the autonomic nervous system, J. Ginseng Res. 38 (2014) 97–105.

[75] S. Bresson, M. El Marssi, B. Khelifa, Raman spectroscopy investigation of various saturated monoacid triglycerides, Chem. Phys. Lipids 134 (2005) 119–129.

[76] O. Samek, A. Jonáš, Z. Pilát, et al., Raman microspectroscopy of individual algal cells: Sensing unsaturation of storage lipids in vivo, Sensors (Basel) 10 (2010) 8635–8651.

[77] Y. Nojima, T. Takaya, K. Iwata, Energy transfer characteristics of lipid bilayer membranes of liposomes examined with picosecond time-resolved Raman spectroscopy, J. Phys. Chem. B 127 (2023) 6684–6693.

[78] E. Bik, N. Mielniczek, M. Jarosz, et al., Tunicamycin induced endoplasmic reticulum changes in endothelial cells investigated in vitro by confocal Raman imaging, Analyst 144 (2019) 6561–6569.

[79] C. Krafft, L. Neudert, T. Simat, et al., Near infrared Raman spectra of human brain lipids, Spectrochim. Acta A Mol. Biomol. Spectrosc. 61 (2005) 1529–1535.

[80] L.J. Dolch, C. Rak, G. Perin, et al., A palmitic acid elongase affects eicosapentaenoic acid and plastidial monogalactosyldiacylglycerol levels in Nannochloropsis, Plant Physiol. 173 (2017) 742–759.

[81] K. Shirota, K. Yagi, T. Inaba, et al., Detection of sphingomyelin clusters by Raman spectroscopy, Biophys. J. 111 (2016) 999–1007.

[82] X. Liu, S. Guo, T. Bocklitz, et al., Nondestructive 3D imaging and quantification of hydrated biofilm matrix by confocal Raman microscopy coupled with non-negative matrix factorization, Water Res. 210 (2022), 117973.

[83] J. Zhang, Q. Li, Y. Wu, et al., Cholesterol content in cell membrane maintains surface levels of ErbB2 and confers a therapeutic vulnerability in ErbB2-positive breast cancer, Cell Commun. Signal. 17 (2019), 15.

[84] K. Zhang, T. Li, X. Shan, et al., Cholesterol: Bioactivities, structural modification, mechanisms of action, and structure-activity relationships, Mini Rev. Med. Chem. 21 (2021) 1830−1848.

[85] M. Pu, W. Zheng, H. Zhang, et al., ORP8 acts as a lipophagy receptor to mediate lipid droplet turnover, Protein Cell 14 (2023) 653−667.

[86] J.A. Olzmann, P. Carvalho, Dynamics and functions of lipid droplets, Nat. Rev. Mol. Cell Biol. 20 (2019) 137−155.

[87] F.X. Xu, G.N. Ioannou, S.P. Lee, et al., Discrimination of lipid composition and cellular localization in human liver tissues by stimulated Raman scattering microscopy, J. Biomed. Opt. 29 (2024), 016008.

[88] S. Oh, C. Lee, W. Yang, et al., Protein and lipid mass concentration measurement in tissues by stimulated Raman scattering microscopy, Proc. Natl. Acad. Sci. USA 119 (2022), e2117938119.

[89] Y. Shen, F. Hu, W. Min, Raman imaging of small biomolecules, Annu. Rev. Biophys. 48 (2019) 347−369.

[90] E. Scorletti, R.M. Carr, A new perspective on NAFLD: Focusing on lipid droplets, J. Hepatol. 76 (2022) 934−945.

[91] A.L.S. Cruz, E. de A Barreto, N.P.B. Fazolini, et al., Lipid droplets: Platforms with multiple functions in cancer hallmarks, Cell Death Dis. 11 (2020), 105.

[92] X. Nan, J. Cheng, X. Sunney Xie, Vibrational imaging of lipid droplets in live fibroblast cells with coherent anti-Stokes Raman scattering microscopy, J. Lipid Res. 44 (2003) 2202−2208.

[93] C. Zhang, S.A. Boppart, Dynamic signatures of lipid droplets as new markers to quantify cellular metabolic changes, Anal. Chem. 92 (2020) 15943−15952.

[94] H. Jia, S. Yue, Stimulated Raman scattering imaging sheds new light on lipid droplet biology, J. Phys. Chem. B 127 (2023) 2381−2394.

[95] Y.C. Kao, P.C. Ho, Y. Tu, et al., Lipids and Alzheimer's disease, Int. J. Mol. Sci. 21 (2020), 1505.

[96] L. Opilik, T. Bauer, T. Schmid, et al., Nanoscale chemical imaging of segregated lipid domains using tip-enhanced Raman spectroscopy, Phys. Chem. Chem. Phys. 13 (2011) 9978−9981.

[97] E.O. Potma, X. Sunney Xie, Direct visualization of lipid phase segregation in single lipid bilayers with coherent anti-Stokes Raman scattering microscopy, Chemphyschem 6 (2005) 77−79.

[98] T. Minamikawa, H. Niioka, T. Araki, et al., Real-time imaging of laser-induced membrane disruption of a living cell observed with multifocus coherent anti-Stokes Raman scattering microscopy, J. Biomed. Opt. 16 (2011), 021111.

[99] G. Zito, G. Rusciano, G. Pesce, et al., Surface-enhanced Raman imaging of cell membrane by a highly homogeneous and isotropic silver nanostructure, Nanoscale 7 (2015) 8593−8606.

[100] G. Pezzotti, S. Horiguchi, F. Boschetto, et al., Raman imaging of individual membrane lipids and deoxynucleoside triphosphates in living neuronal cells during neurite outgrowth, ACS Chem. Neurosci. 9 (2018) 3038−3048.

[101] D. Zhang, Y. Feng, Q. Zhang, et al., Raman spectrum reveals the cell cycle arrest of Triptolide-induced leukemic T-lymphocytes apoptosis, Spectrochim. Acta A Mol. Biomol. Spectrosc. 141 (2015) 216−222.

[102] A. Ali, Y. Abouleila, A. Germond, An integrated Raman spectroscopy and mass spectrometry platform to study single-cell drug uptake, metabolism, and effects, J. Vis. Exp. 155 (2020).

[103] I. Pope, F. Masia, K. Ewan, et al., Identifying subpopulations in multicellular systems by quantitative chemical imaging using label-free hyperspectral CARS microscopy, Analyst 146 (2021) 2277−2291.

[104] C. Li, J. Ruan, M. Yang, et al., Human induced pluripotent stem cells labeled with fluorescent magnetic nanoparticles for targeted imaging and hyperthermia therapy for gastric cancer, Cancer Biol. Med. 12 (2015) 163−174.

[105] S.A. Choi, Y.H. Kim, Y.H. Park, et al., Novel crosstalk between Vps26a and Nox4 signaling during neurogenesis, Cell Death Differ. 26 (2018) 1582−1599.

[106] W. Du, S. Amarachintha, J. Sipple, et al., Inflammation-mediated Notch signaling skews fanconi *Anemia* hematopoietic stem cell differentiation, J. Immunol. 191 (2013) 2806−2817.

[107] A. Alraies, E. Canetta, R.J. Waddington, et al., Discrimination of dental pulp stem cell regenerative heterogeneity by single-cell Raman spectroscopy, Tissue Eng. Part C Methods 25 (2019) 489−499.

[108] C.C. Hsu, J. Xu, B. Brinkhof, et al., A single-cell Raman-based platform to identify developmental stages of human pluripotent stem cell-derived neurons, Proc. Natl. Acad. Sci. USA 117 (2020) 18412−18423.

[109] I.R. Suhito, Y. Han, Y.S. Ryu, et al., Autofluorescence-Raman Mapping Integration analysis for ultra-fast label-free monitoring of adipogenic differentiation of stem cells, Biosens. Bioelectron. 178 (2021) 113018.

[110] J.S. Choi, Y. Ilin, M.L. Kraft, et al., Tracing hematopoietic progenitor cell neutrophilic differentiation *via* Raman spectroscopy, Bioconjug. Chem. 29 (2018) 3121−3128.

[111] J.K. Pijanka, D. Kumar, T. Dale, et al., Vibrational spectroscopy differentiates between multipotent and pluripotent stem cells, Analyst 135 (2010) 3126−3132.

[112] A. Germond, Y. Panina, M. Shiga, et al., Following embryonic stem cells, their differentiated progeny, and cell-state changes during iPS reprogramming by Raman spectroscopy, Anal. Chem. 92 (2020) 14915−14923.

[113] J. Simonović, B. Toljić, B. Rašković, et al., Raman microspectroscopy: Toward a better distinction and profiling of different populations of dental stem cells, Croat. Med. J. 60 (2019) 78−86.

[114] T. Kukolj, J. Lazarević, A. Borojević, et al., A single-cell Raman spectroscopy analysis of bone marrow mesenchymal stem/stromal cells to identify inter-individual diversity, Int. J. Mol. Sci. 23 (2022), 4915.

[115] L. Harkness, S.M. Novikov, J. Beermann, et al., Identification of abnormal stem cells using Raman spectroscopy, Stem Cells Dev. 21 (2012) 2152−2159.

[116] A.E. Pollard, D. Carling, Thermogenic adipocytes: Lineage, function and therapeutic potential, Biochem. J. 477 (2020) 2071−2093.

[117] M. Cedikova, M. Kripnerová, J. Dvorakova, et al., Mitochondria in white, brown, and beige adipocytes, Stem Cells Int. 2016 (2016), 6067349.

[118] W. Wang, P. Seale, Control of brown and beige fat development, Nat. Rev. Mol. Cell Biol. 17 (2016) 691−702.

[119] J. Tratwal, G. Falgayrac, A. During, et al., Raman microspectroscopy reveals unsaturation heterogeneity at the lipid droplet level and validates an *in vitro* model of bone marrow adipocyte subtypes, Front. Endocrinol. (Lausanne) 13 (2022), 1001210.

[120] T. Yamaguchi, N. Omatsu, E. Morimoto, et al., CGI-58 facilitates lipolysis on lipid droplets but is not involved in the vesiculation of lipid droplets caused by hormonal stimulation, J. Lipid Res. 48 (2007) 1078−1089.

[121] M. Paar, C. Jüngst, N.A. Steiner, et al., Remodeling of lipid droplets during lipolysis and growth in adipocytes, J. Biol. Chem. 287 (2012) 11164−11173.

[122] T. Hashimoto, H. Segawa, M. Okuno, et al., Active involvement of micro-lipid droplets and lipid-droplet-associated proteins in hormone-stimulated lipolysis in adipocytes, J. Cell Sci. 125 (2012) 6127−6136.

[123] C.M. Hsieh, P.Y. Liu, L.K. Chin, et al., Regulation of lipid droplets in live preadipocytes using optical diffraction tomography and Raman spectroscopy, Opt. Express 27 (2019) 22994−23008.

[124] S. Zhang, Y. He, S. Yue, Coherent Raman scattering imaging of lipid metabolism in cancer, J. Innov. Opt. Health Sci. 16 (2023), 2230015.

[125] Y. Takei, R. Hirai, A. Fukuda, et al., Visualization of intracellular lipid metabolism in brown adipocytes by time-lapse ultra-multiplex CARS microspectroscopy with an onstage incubator, J. Chem. Phys. 155 (2021), 125102.

[126] E. Świderska, M. Podolska, J. Strycharz, et al., Hyperglycemia changes expression of key adipogenesis markers *(C/EBPα and PPARγ)* and morphology of differentiating human visceral adipocytes, Nutrients 11 (2019), 1835.

[127] Z. Majka, K. Czamara, J. Janus, et al., Prominent hypertrophy of perivascular adipocytes due to short-term high fat diet, Biochim. Biophys. Acta Mol. Basis Dis. 1868 (2022), 166315.

[128] E. Stanek, K. Czamara, A. Kaczor, Increased obesogenic action of palmitic acid during early stage of adipogenesis, Biochim. Biophys. Acta Mol. Cell Biol. Lipids 1869 (2024), 159525.

[129] M. Kopec, K. Beton-Mysur, H. Abramczyk, Raman imaging and chemometric methods in human normal bronchial and cancer lung cells: Raman biomarkers of lipid reprogramming, Chem. Phys. Lipids 257 (2023), 105339.

[130] M. Hedegaard, C. Krafft, H.J. Ditzel, et al., Discriminating isogenic cancer cells and identifying altered unsaturated fatty acid content as associated with metastasis status, using k-means clustering and partial least squares-discriminant analysis of Raman maps, Anal. Chem. 82 (2010) 2797−2802.

[131] G. Rappa, J. Mercapide, F. Anzanello, et al., Wnt interaction and extracellular release of prominin-1/CD133 in human malignant melanoma cells, Exp. Cell Res. 319 (2013) 810−819.

[132] H.J. Wright, J. Hou, B. Xu, et al., CDCP1 drives triple-negative breast cancer metastasis through reduction of lipid-droplet abundance and stimulation of fatty acid oxidation, Proc. Natl. Acad. Sci. USA 114 (2017) E6556−E6565.

[133] H.M. Kang, K.H. Noh, T.K. Chang, et al., Ubiquitination of MAP1LC3B by pVHL is associated with autophagy and cell death in renal cell carcinoma, Cell Death Dis. 10 (2019), 279.

[134] S. Zhang, T. Fang, Y. He, et al., VHL mutation drives human clear cell renal cell carcinoma progression through PI3K/AKT-dependent cholesteryl ester accumulation, EBioMedicine 103 (2024), 105070.

[135] C. Steuwe, I.I. Patel, M. Ul-Hasan, et al., CARS based label-free assay for assessment of drugs by monitoring lipid droplets in tumour cells, J. Biophotonics 7 (2014) 906−913.

[136] R. Poojari, M. Bhujbal, A. Hole, et al., Distinct stratification of normal liver, hepatocellular carcinoma (HCC), and anticancer nanomedicine-treated- tumor tissues by Raman fingerprinting for HCC therapeutic monitoring, Nanomedicine 33 (2021), 102352.

[137] M. Roman, T.P. Wrobel, A. Panek, et al., Lipid droplets in prostate cancer cells and effect of irradiation studied by Raman microspectroscopy, Biochim. Biophys. Acta Mol. Cell Lipids 1865 (2020), 158753.

[138] X. Bi, X. Rexer, C.L. Arteaga, et al., Evaluating HER2 amplification status and acquired drug resistance in breast cancer cells using Raman spectroscopy, J. Biomed. Opt. 19 (2014), 025001.

[139] L.E. Jamieson, C. Wetherill, K. Faulds, et al., Ratiometric Raman imaging reveals the new anti-cancer potential of lipid targeting drugs, Chem. Sci. 9 (2018) 6935−6943.

[140] M.C. Potcoava, G.L. Futia, J. Aughenbaugh, et al., Raman and coherent anti-Stokes Raman scattering microscopy studies of changes in lipid content and composition in hormone-treated breast and prostate cancer cells, J. Biomed. Opt. 19 (2014), 111605.

[141] M.A. de la Rosa Rodriguez, L. Deng, A. Gemmink, et al., Hypoxia-inducible lipid droplet-associated induces DGAT1 and promotes lipid storage in hepatocytes, Mol. Metab. 47 (2021), 101168.

[142] M.B. Schott, S.G. Weller, R.J. Schulze, et al., Lipid droplet size directs lipolysis and lipophagy catabolism in hepatocytes, J. Cell Biol. 218 (2019) 3320−3335.

[143] T. Minamikawa, M. Ichimura-Shimizu, H. Takanari, et al., Molecular imaging analysis of microvesicular and macrovesicular lipid droplets in non-alcoholic fatty liver disease by Raman microscopy, Sci. Rep. 10 (2020), 18548.

[144] I.W. Schie, J. Wu, T. Weeks, et al., Label-free imaging and analysis of the effects of lipolysis products on primary hepatocytes, J. Biophotonics 4 (2011) 425−434.

[145] P.N. Paramitha, R. Zakaria, A. Maryani, et al., Raman study on lipid droplets in hepatic cells co-cultured with fatty acids, Int. J. Mol. Sci. 22 (2021), 7378.

[146] C. Ma, L. Zhang, T. He, et al., Single cell Raman spectroscopy to identify different stages of proliferating human hepatocytes for cell therapy, Stem Cell Res. Ther. 12 (2021), 555.

[147] R. Aizawa, M. Ibayashi, J. Mitsui, et al., Lipid droplet formation is spatio-temporally regulated in oocytes during follicular development in mice, J. Reprod. Dev. 70 (2024) 18−24.

[148] R. Arena, S. Bisogno, Ł. Gąsior, et al., Lipid droplets in mammalian eggs are utilized during embryonic diapause, Proc. Natl. Acad. Sci. USA 118 (2021), e2018362118.

[149] B. Davidson, A.A. Murray, A. Elfick, et al., Raman micro-spectroscopy can be used to investigate the developmental stage of the mouse oocyte, PLoS One 8 (2013), e67972.

[150] K.A. Okotrub, V.I. Mokrousova, S.Y. Amstislavsky, et al., Lipid droplet phase transition in freezing cat embryos and oocytes probed by Raman spectroscopy, Biophys. J. 115 (2018) 577−587.

[151] K.A. Okotrub, S.V. Okotrub, V.I. Mokrousova, et al., Lipid phase transitions in cat oocytes supplemented with deuterated fatty acids, Biophys. J. 120 (2021) 5619−5630.

[152] K.A. Okotrub, A.N. Omelchenko, E.A. Chuyko, et al., Irreversible lipid phase transition detected in a porcine oocyte at chilling, Cryobiology 114 (2024), 104850.

[153] S. Xu, S. Offermanns, Endothelial lipid droplets drive atherosclerosis and arterial hypertension, Trends Endocrinol. Metab. 35 (2024) 453−455.

[154] B. Kim, W. Zhao, S.Y. Tang, et al., Endothelial lipid droplets suppress ENOS to link high fat consumption to blood pressure elevation, J. Clin. Invest. 133 (2023), e173160.

[155] K. Majzner, K. Kochan, N. Kachamakova-Trojanowska, et al., Raman imaging providing insights into chemical composition of lipid droplets of different size and origin: In hepatocytes and endothelium, Anal. Chem. 86 (2014) 6666−6674.

[156] K. Majzner, S. Tott, L. Roussille, et al., Uptake of fatty acids by a single endothelial cell investigated by Raman spectroscopy supported by AFM, Analyst 143 (2018) 970−980.

[157] M.Z. Pacia, K. Majzner, K. Czamara, et al., Estimation of the content of lipids composing endothelial lipid droplets based on Raman imaging, Biochim. Biophys. Acta Mol. Cell Biol. Lipids 1865 (2020), 158758.

[158] M. Baranska, A. Kaczor, K. Malek, et al., Raman microscopy as a novel tool to detect endothelial dysfunction, Pharmacol. Rep. 67 (2015) 736−743.

[159] B. Radwan, A. Adamczyk, S. Tott, et al., Labeled vs. label-free Raman imaging of lipids in endothelial cells of various origins, Molecules 25 (2020), 5752.

[160] B. Radwan, A. Prabhakaran, S. Rocchetti, et al., Uptake and anti-inflammatory effects of liposomal astaxanthin on endothelial cells tracked by Raman and fluorescence imaging, Mikrochim. Acta 190 (2023), 332.

[161] A. Al Saedi, D.A. Debruin, A. Hayes, et al., Lipid metabolism in sarcopenia, Bone 164 (2022), 116539.

[162] S. Daemen, A. Gemmink, A. Paul, et al., Label-free CARS microscopy reveals similar triacylglycerol acyl chain length and saturation in myocellular lipid droplets of athletes and individuals with type 2 diabetes, Diabetologia 63 (2020) 2654−2664.

[163] S. Daemen, A. Gemmink, B. Brouwers, et al., Distinct lipid droplet characteristics and distribution unmask the apparent contradiction of the athlete's paradox, Mol. Metab. 17 (2018) 71−81.

[164] T. Wu, J. Li, S. Zheng, et al., Magnetic nanotag-based colorimetric/SERS dual-readout immunochromatography for ultrasensitive detection of clenbuterol hydrochloride and ractopamine in food samples, Biosensors (Basel) 12 (2022), 709.

[165] A. Sasso, A. Capaccio, G. Rusciano, Exploring reliable and efficient plasmonic nanopatterning for surface- and tip-enhanced Raman spectroscopies, Int. J. Mol. Sci. 24 (2023), 16164.

[166] K. Qiu, Y. Du, J. Liu, et al., Super-resolution observation of lysosomal dynamics with fluorescent gold nanoparticles, Theranostics 10 (2020) 6072−6081.

[167] M. Jensen, S. Liu, E. Stepula, et al., Opto-lipidomics of tissues, Adv. Sci. 11 (2024), e2302962.

[168] L.M. Sherman, A.P. Petrov, L.F.P. Karger, et al., A surface-enhanced Raman spectroscopy database of 63 metabolites, Talanta 210 (2020), 120645.

[169] Y. Li, D.K.J. Lee, P. Cai, et al., A database of computed Raman spectra of inorganic compounds with accurate hybrid functionals, Sci. Data 11 (2024), 105.

[170] S. Gao, Y. Lin, X. Zhao, et al., Label-free surface enhanced Raman spectroscopy analysis of blood serum via coffee ring effect for accurate diagnosis of cancers, Spectrochim. Acta A Mol. Biomol. Spectrosc. 267 (2022), 120605.

[171] E. Cordero, I. Latka, C. Matthäus, et al., In-vivo Raman spectroscopy: From basics to applications, J. Biomed. Opt. 23 (2018) 1−23.

[172] Z. Majka, K. Czamara, P. Wegrzyn, et al., A new approach to study human perivascular adipose tissue of the internal mammary artery by fiber-optic Raman spectroscopy supported by spectral modelling, Analyst 146 (2021) 270−276.

[173] C.C. Horgan, M.S. Bergholt, M.Z. Thin, et al., Image-guided Raman spectroscopy probe-tracking for tumor margin delineation, J. Biomed. Opt. 26 (2021), 036002.

[174] I.A. Bratchenko, L.A. Bratchenko, A.A. Moryatov, et al., In vivo diagnosis of skin cancer with a portable Raman spectroscopic device, Exp. Dermatol. 30 (2021) 652−663.

[175] I. Pence, A. Mahadevan-Jansen, Clinical instrumentation and applications of Raman spectroscopy, Chem. Soc. Rev. 45 (2016) 1958−1979.